

Next-Generation Seismic Experiments: Wide-Angle, Multi-Azimuth, 3D, Full-Waveform  
Inversion

Joanna Morgan<sup>1</sup>, Michael Warner<sup>1</sup>, Rebecca Bell<sup>1</sup>, Jack Ashley<sup>1</sup>, Danielle Barnes<sup>1</sup>, Rachel  
Little<sup>1</sup>, Katarina Roele<sup>1</sup>, and Charles Jones<sup>2</sup>

1 Department of Earth Science and Engineering, Imperial College London, SW7 2AZ, UK.

2 BG Group, Reading, Berkshire RG6 1PT UK

Abbreviated title: Next-Generation Seismic Experiments

Contact author: Joanna Morgan, j.morgan@imperial.ac.uk, 0207 5946423

**Key Words:** controlled source seismology, seismic tomography, continental margins:  
divergent, volcanic arc processes, crustal structure

## SUMMARY

Full-waveform inversion (FWI) is an advanced seismic imaging technique that has recently become computationally feasible in three dimensions, and that is being widely adopted and applied by the oil and gas industry. Here we explore the potential for 3D FWI, when combined with appropriate marine seismic acquisition, to recover high-resolution high-fidelity P-wave velocity models for sub-sedimentary targets within the crystalline crust and uppermost mantle. We demonstrate that FWI is able to recover detailed three-dimensional structural information within a radially faulted dome using a field dataset acquired with a standard 3D petroleum-industry marine acquisition system. Acquiring low-frequency seismic data is important for successful FWI; we show that current acquisition techniques can routinely acquire field data from airguns at frequencies as low as 2 Hz, and that 1 Hz acquisition is likely to be achievable using ocean-bottom hydrophones in deep water. Using existing geological and geophysical models, we construct P-wave velocity models over three potential sub-sedimentary targets: the Soufrière Hills Volcano on Montserrat and its associated crustal magmatic system, the crust and uppermost mantle across the continent-ocean transition beneath the Campos Basin offshore Brazil, and the oceanic crust and uppermost mantle beneath the East Pacific Rise mid-ocean ridge. We use these models to generate realistic multi-azimuth 3D synthetic seismic data, and attempt to invert these data to recover the original models. We explore resolution and accuracy, sensitivity to noise and acquisition geometry, ability to invert elastic data using acoustic inversion codes, and the trade-off between low frequencies and starting velocity model accuracy. We show that FWI applied to multi-azimuth, refracted, wide-angle, low-frequency data can resolve features in the deep crust and uppermost mantle on scales that are significantly better than can be achieved by any other geophysical technique, and that these results can be obtained using relatively small numbers (60 – 90) of ocean-bottom receivers combined with large numbers of airgun shots. We demonstrate that multi-azimuth 3D FWI is robust in the presence of noise, that acoustic FWI can invert elastic data successfully, and that the typical errors to be expected in starting models derived using travel-times will not be problematic for FWI given appropriately designed acquisition. FWI is a rapidly maturing technology; its transfer from the petroleum sector to tackle a much broader range of targets now appears to be entirely achievable.

# 1 INTRODUCTION

2 Three-dimensional full-waveform inversion (FWI) of wide-angle seismic data is a newly  
3 practical technique that has advanced rapidly within the oil and gas industry, see for example  
4 Sirgue *et al.* (2010), Kapoor *et al.* (2013), Warner *et al.* (2013a). In this paper, we explore  
5 the potential for this computationally demanding technique to address larger-scale problems  
6 within the sub-sedimentary crystalline crust and shallowest upper mantle that have  
7 applications both within and well beyond the interests of the petroleum industry.

8 Three-dimensional seismic reflection surveys currently provide the highest-resolution images  
9 of the Earth's sedimentary layers, and form the principal geophysical tool that is used in the  
10 exploration for and exploitation of commercial hydrocarbons. Using seismic reflection data,  
11 images of sedimentary horizons and structures are produced, that can be tracked across  
12 basins to provide maps and models with a vertical resolution of a few tens of metres. In  
13 some circumstances however, when the potential targets lie beneath complex overburden,  
14 3D reflection methods can fail to provide sufficiently high-fidelity images of the target.

15 Recently, 3D iterative inversion of the pre-stack seismic wavefield has been used to obtain  
16 high-resolution velocity models, which have subsequently led to significant improvements in  
17 the migration of reflections from deeper targets (for example Houbiers *et al.* 2013, Selwood  
18 *et al.* 2013). This application of three-dimensional full-waveform inversion, to obtain an  
19 accurate velocity model over a wide range of length scales, has been particularly successful  
20 in improving depth-migrated images of petroleum reservoirs that lie beneath heterogeneous  
21 gas clouds (e.g. Sirgue *et al.* 2010; Ratcliffe *et al.* 2012), buried fluvial channels (e.g. Warner  
22 *et al.* 2013a), salt bodies (e.g. Plessix & Perkins 2010; Kapoor *et al.* 2012), faulted domes  
23 (e.g. Jones *et al.* 2013), and other structurally and lithologically complex overburden. In this  
24 application of FWI, the inversion is driven predominantly by the low-frequency transmitted  
25 wavefield (Virieux & Operto 2009), which has a typical penetration depth of around a third to  
26 a sixth of the maximum source-receiver offset. Conventional surface-streamer and ocean-  
27 bottom-cable data have limited offsets which means that the transmitted wavefield may not  
28 penetrate to the target depth of interest, particularly in deep water and for deep targets.

29 Here we explore the application of this rapidly maturing technology to investigate a wider  
3

range of sub-sedimentary targets. In particular, we assess the potential of three-dimensional, wide-angle, long-offset, low-frequency FWI as a tool to determine P-wave velocity structure beneath an active arc-volcano, within the crystalline upper and lower crust across a passive continental margin, and across an active ocean-spreading centre. In petroleum applications, the main commercial use of FWI is currently to improve subsequent depth migration of deeper reflectors. In this study however, and increasingly within the petroleum industry, our interest is in recovering and then interpreting the FWI velocity model directly.

## FULL-WAVEFORM INVERSION

Full-waveform inversion seeks to find a high-resolution high-fidelity quantitative model of the subsurface that is capable of predicting the seismic field data, wiggle-for-wiggle, trace-by-trace. Although in principle FWI can be used to recover any subsurface property that influences the recorded seismic wavefield (e.g. Prieux *et al.* 2013), in commercial applications it is most often only the P-wave velocity model that is recovered. The method involves iteratively updating an initial starting model, using a linearized local inversion, to solve the full non-linear inversion problem. Pratt (1999) presents the underlying theory, and Pratt *et al.* (1996) show an early application of the method to crustal-scale targets. The principal benefit of FWI is that it has the potential to resolve sub-surface properties to about half the seismic wavelength (Virieux & Operto 2009), and this is a significant improvement on conventional travel-time tomography for which the resolution is limited to be approximately a Fresnel width (Williamson 1991), that is the resolution is of the order of the square root of the product of the seismic wavelength and the length of the ray path.

The underlying theory was first outlined by Tarantola (1984), and a detailed recent review of FWI can be found in Virieux & Operto (2009). Early applications of FWI were in 2D (e.g. Pratt *et al.* 1996; Pratt & Shipp 1999; Shipp & Singh, 2002), but 3D inversion has superior convergence and accuracy (Virieux & Operto, 2009; Sirgue *et al.* 2010), and is in any case vital for imaging targets with significant structural complexity. In particular, sampling the subsurface in three dimensions with multi-azimuth multiply-crossing wavefields leads to a significantly improved recovery of sub-surface velocities (Sirgue *et al.* 2007; Plessix 2008;

1 Mothi *et al.* 2013). In contrast, two-dimensional inversion can only explain out-of-plane  
2 arrivals by mapping them into in-plane artefacts (Morgan *et al.* 2009), and two-dimensional  
3 acquisition provides much more limited coverage of all portions of the sub-surface. FWI is a  
4 tomographic method that achieves its resolving power by being able to combine many  
5 independent observations of each region of a model. In three dimensions, using multi-  
6 azimuth acquisition, many more independent observations can be made for each portion of  
7 the sub-surface than is possible using a narrow-azimuth 3D or single-azimuth 2D acquisition  
8 geometry. Two-dimensional FWI however remains important as it is significantly less  
9 computationally intensive, and so allows a detailed exploration of the parameter space prior  
10 to 3D inversion. In this paper, we consider only 3D FWI, and we consider explicitly only  
11 those methods that have become well-established within the petroleum industry, and that  
12 have been validated using 3D field data in combination with direct sub-surface  
13 measurements in boreholes.

14 In principle, FWI can be applied to invert forward-scattered, transmitted, refracted arrivals, or  
15 back-scattered, sub-critical, reflected arrivals. FWI can also of course use both types of data  
16 together, and in reality there is a continuum from one data type to the other that includes  
17 wide-angle and post-critical reflections, back-scattered refractions, and the transmitted  
18 portion of reflected phases. In practice though, these two generic data types can often be  
19 usefully distinguished, and are often dealt with differently and separately. Conventional  
20 reflection imaging uses only sub-critical, relatively-short-offset, reflected arrivals, whereas  
21 conventional transmission FWI typically uses only, or predominantly, the post-critical, long-  
22 offset, refracted arrivals.

23 It is possible to apply FWI directly to sub-critical reflection data (e.g. Xu *et al.* 2012), but that  
24 is not yet common practice within the petroleum industry. Reflection FWI, as described  
25 initially by Tarantola (1984), has proven to be much more sensitive to the sub-wavelength  
26 variation in physical properties across individual reflectors than it is to the wavelength and  
27 larger-scale macro-velocity model (Sambridge & Mosegaard, 2002; Virieux & Operto, 2009).  
28 As a consequence of this, commercial FWI of 3D reflection data has been limited thus far to  
29 produce what are essentially reverse-time migration images of reflection events into pre-  
30 existing macro velocity models (e.g. Vigh *et al.* 2010), or to produce very-high-resolution

1 models of impedance contrasts superimposed upon an already highly accurate and well-  
2 resolved macro velocity model that will have been typically developed using sonic  
3 measurements from wells within the imaged volume (e.g. Lazaratos *et al.* 2011). Both these  
4 can be useful applications, but they are not the approach that has been widely adopted  
5 across the industry, and these reflection methods are not currently able to update macro-  
6 velocity models in a meaningful way.

7 FWI, as it has come to be predominantly applied across the petroleum industry (e.g. Sirgue  
8 *et al.* 2010; Vigh *et al.* 2011; Prieux *et al.* 2013), uses wide-angle, long-offset, low-frequency  
9 datasets that are dominated by forward-scattered, refracted, transmitted arrivals (Vigh *et al.*  
10 2013a; Mothi *et al.* 2013). With few exceptions, commercial FWI uses an acoustic  
11 approximation to the wave equation (Virieux & Operto, 2009; Kapoor *et al.* 2013), and it  
12 commonly includes the kinematic effects of P-wave anisotropy (Selwood *et al.* 2013; Warner  
13 *et al.* 2013a). With appropriate acquisition, this form of FWI is capable of updating the  
14 macro-velocity model at all length scales ranging from the full extent of the model down to  
15 about half the seismic wavelength; we demonstrate updates on both these length scales in  
16 field and synthetic examples below. Throughout the remainder of this paper, we are  
17 concerned only with this approach to wide-angle transmission FWI. The workflows, data pre-  
18 processing, algorithms, software, rationale and overall approach that we have applied to both  
19 field and synthetic data here follow closely those described in Warner *et al.* (2013a).

20 Full-waveform inversion can be implemented in a number of ways. Here, we model and  
21 invert exclusively in the time domain. Throughout this paper, where we state particular  
22 frequencies at which we invert, these refer to the cut-off frequency of a low-pass filter; in all  
23 cases we invert finite-bandwidth data. During inversion of field data, we invariably normalise  
24 trace amplitudes; that is, we scale the RMS amplitude of the predicted data so that it  
25 matches that of the field data, trace-by-trace. In the time domain FWI, this form of trace  
26 amplitude normalisation is not equivalent to the phase-only inversion that is commonly  
27 performed in the frequency domain (e.g. Pratt & Shipp, 1999).

28 In the time domain, our method predicts and matches both the amplitude and phase spectra  
29 of every trace over the bandwidth of the pre-processed data, and it matches the waveform of

every trace over that bandwidth. The one parameter, for each trace, that we do not seek to match during the inversion is a single scalar for the amplitude spectrum, or equivalently a single scalar multiplier for the time-domain trace. Since the inversion, as we formulate it here, typically takes no account of anelastic attenuation, sub-resolution scattering, or elastic effects, and since we do not know or independently invert for the density model, the use of absolute amplitudes is unhelpful; if they are included, then they serve principally to map the effects of the unknown parameters into the P-wave velocity field. Amplitude normalisation of the raw seismic data has proven to be largely effective in suppressing this undesirable effect (Warner *et al.* 2013a), and its use is now standard practice during wide-angle commercial FWI of 3D field data (personal communication: P Williamson, TOTAL; A Brenders, BP; A Ratcliffe, CGG). We therefore follow this same approach when we invert synthetic data. We emphasise however that we do invert for, and match, the individual waveforms of the field data. That is, we seek to match the detailed shape of the entire seismic trace after pre-processing, and we invert for the correct shape of both the amplitude and phase spectra of every trace.

In synthetic studies, especially in 2D, it is possible to invert using very large numbers of iterations, driving the residual data down to a small fraction of its initial value, and recovering the fine details of the original velocity model to almost any level of precision. This approach however is not normally possible with field data where it is uncommon for the residual to drop by as much as half of its initial value, and where it is seldom cost effective or even affordable in principle to run many thousands of iterations in three dimensions. Consequently here, we invert synthetic data using as far as possible the same approach that we would adopt with a field dataset, and we invert using only a few tens of iterations.

The cost of 3D FWI scales as the fourth power of the maximum frequency used, and so, while the cost of inverting field data is easy to justify, the cost of running synthetic experiments at high frequencies is not. Elapsed times for the acoustic inversions of synthetic data that we use below, when inverting frequencies up to about 6.5 Hz, range from a few to many hours depending upon the size of the model and the size of the seismic dataset when running on around 400 cores. Working up to 25 Hz, which we have done on field data, increases the elapsed time for these inversions so that they would take from one to several

months elapsed time on the same hardware. This is a small cost for a field dataset when compared to the cost of data acquisition, but it is a large cost for synthetic studies that necessarily involve many such runs. Consequently we here restrict our synthetic inversions only to lower frequencies; extension to higher frequencies is straightforward and serves principally to increase the spatial resolution in direct proportion to the maximum frequency and shortest wavelength used during the inversion.

## FIELD EXAMPLE

We begin by demonstrating what can be achieved by applying transmission FWI to a conventional 3D field dataset from the petroleum industry. The data that we consider were acquired as part of a towed-streamer marine-airgun survey, shot in a water depth of about 250 m, using a conventional 3D commercial acquisition seismic vessel, over the Samson Dome in the Barents Sea, offshore Norway (Jones *et al.* 2013). The top of the dome has been removed by a significant erosional unconformity, and it is overlain by Quaternary sediments, including areas of high amplitude potentially associated with shallow gas. This complex geology in the shallow section, in combination with significant radial faulting at the crest of the dome below the unconformity, has the potential for large, rapid velocity variations.

The total full-fold survey area covered about 1000 km<sup>2</sup>. The acquisition was simple narrow-azimuth multi-streamer 3D, employing 10 surface streamers, each 6000 m long, separated laterally by 100 m, employing dual flip-flop sources fired at 12.5 m intervals inline, with 500 m laterally between sail lines. The nominal source and receiver depths were 5 m and 7 m respectively. No low-cut field filters were employed, but no other special attempt was made to generate or record unusually low frequencies during the survey. Prior to FWI, the raw shot records had swell noise attenuation and linear radon de-noise processes applied to improve the signal-to-ambient-noise ratio. The data were low-pass filtered using a 7 Hz high-cut, and top and bottom mutes were applied to retain only the P-wave transmitted energy. No double-converted shear-waves are visible on the field data. No demultiple or deghosting was applied. Only every fourth shot point was retained during the inversion to give a 50 m inline and 500 m cross line source spacing.



FWI requires a good starting velocity model and a good estimate of the source wavelet. In this study, this starting velocity model was obtained using a constrained Dix inversion of the pre-stack time-migration RMS velocity field, stretched to depth, and combined with a one-dimensional blocky model of anisotropy obtained by matching to the single well that penetrates this structure. The source wavelet was obtained by modelling the known characteristics of the airgun array. The pre-processing, starting-model building, and source determination used only relatively simple and well-established techniques that are in routine use within the petroleum industry. In particular, building the starting model was not unduly time-consuming or difficult.

Fig. 1a shows horizontal slices through the starting velocity model. The circular structure is the Samson Dome, and many of the fine details in this starting model are unlikely to reflect reality accurately; they result principally from uncertainties in the RMS velocities that become magnified when these are converted to interval velocities using the Dix equation. Three-dimensional acoustic anisotropic time-domain FWI was run on the pre-processed transmission data using the computer codes and approach described by Warner *et al.* (2013). Early iterations used a restricted bandwidth that began at 2 Hz, and that was incremented by stages up to the highest-used frequency of 7 Hz. Trace-by-trace amplitude normalisation was applied during FWI to both the predicted and field data.

Fig. 1b shows the results of the inversion. These are the same horizontal slices as were shown for the starting model; the anisotropy model has not been changed, only P-wave velocity is being updated during the inversion. Two features are immediately apparent when comparing Figs 1a and 1b – the long-wavelength background velocity model has changed, and additional short-wavelength structure has appeared. Both these are important characteristics of transmission FWI. The method has updated the model over a wide range of scale lengths, ranging from about half the seismic wavelength up to the scale of the entire model. Two questions immediately arise: is the recovered long-wavelength background-velocity model accurate, and are the highly resolved short-wavelength features real?

The first of these questions is answered by Jones *et al.* (2013). They show that the FWI-recovered velocity model depth migrates deeper short-offset reflection data better than the

1 starting model. That is, the FWI-based migration shows greater reflector continuity, greater  
2 stack power, better signal-to-noise ratio, fewer conflicting dips, and fewer migration artefacts.  
3 They also show that the FWI velocity model better flattens Kirchhoff-migrated common-  
4 image gathers. Both these results indicate that the FWI long-wavelength model is closer to  
5 the true earth model than is the starting model.

6 The second question, which in the present context is the more interesting one, is answered  
7 by Fig. 1c. This shows a depth slice through the migrated reflection volume superimposed  
8 upon the FWI velocity model. The migration and depth conversion of the reflection volume  
9 was performed using the original starting velocity model so that there has been no transfer of  
10 information from the FWI model to the reflection data. The many lineations that cut the dome  
11 in the FWI velocity model in Fig. 1b look like steeply dipping faults. If that is indeed what  
12 they are, then they should also be visible in the reflection data where they would manifest as  
13 offsets, vertically and/or horizontally, in the reflecting horizons across which they cut. Fig. 1c  
14 shows that almost every lineation seen in the velocity model corresponds to the position of  
15 an obvious faulted offset in the reflection data. The reverse is also true; almost every fault  
16 that can be picked on the reflection data also corresponds to a lineation or linear offset in the  
17 FWI velocity model.

18 We note that these two subsurface models – reflectivity and FWI-recovered velocity – are  
19 derived from largely independent subsets of the field data. The former is obtained using  
20 near-normal-incidence reflections from which all the refracted arrivals have been removed,  
21 whereas the latter is derived from the wide-angle refracted arrivals from which (almost) all of  
22 the short-offset reflections have been removed. At the earliest times, these two datasets  
23 cannot be completely separated, but this overlap does not occur at the times and offsets that  
24 generate any of the data and models seen in Fig. 1 – here the reflections and refractions  
25 form distinct and separately processed datasets. Since the two models are independently  
26 derived, the remarkably close agreement between them provides strong evidence that the  
27 short-wavelength FWI-recovered velocity model is accurate as well as being well resolved.

28 Looking more closely at Fig. 1, it is clear that much of the structural information that exists  
29 within the reflection data is also apparent within the FWI velocity model. At the depths

1 shown, it is possible to build a detailed structural model of the dome, and of the faults that  
2 dissect it, in fine detail, using only the FWI velocity model. The velocity model however  
3 contains more than just this structural information since it also provides a quantitative  
4 description of the subsurface rather than simply a qualitative image. Some of the individual  
5 faults represent high-velocity zones, some represent low-velocity zones, some have more  
6 complex internal structure, and some are visible merely as offsets between two blocks with  
7 contrasting velocity. Although it has not yet been demonstrated quantitatively for this  
8 dataset, it seems likely that at least some of this visible fine structure is related to the detailed  
9 lithology, strain history, pore geometry, and fluid properties within the individual faults.

10 In the context of sub-sedimentary crustal FWI, the starting model analogous to Fig. 1a will be  
11 generated by travel-time tomography, Fig. 1b will be generated by FWI applied to wide-  
12 azimuth long-offset ocean-bottom-hydrophone data, and Fig. 1c will typically consist only of  
13 data from a relatively small number of 2D reflections lines. The aim of such sub-sedimentary  
14 experiments and analysis will be to generate the crustal and sub-crustal analogues of Fig.  
15 1b, and to interpret directly the velocity structure that they contain.

## 16 **OBTAINING LOW FREQUENCIES**

17 Wide-angle FWI requires low frequencies within the field data. These are required because  
18 the starting model must be able to reproduce the observed wavefield to within half a cycle of  
19 the lowest inversion frequency in order to avoid cycle skipping (Sirgue 2006). Cycle skipping  
20 occurs when a local inversion scheme modifies the sub-surface model to force a match  
21 between observed and predicted seismic data that occurs one or more cycles removed from  
22 the correct match. This is a significant concern for practical FWI. It is currently overcome by  
23 working initially at (very) low frequency, by building (very) accurate velocity models initially  
24 using travel-time tomography and similar methods, and by layer stripping the model and/or  
25 the data so that shallow parts of the model, or short offsets and early travel times, are  
26 updated first which improves the data match prior to subsequent inversion to recover  
27 successively deeper portions of the model (Virieux & Operto 2009). We adopt this latter  
28 strategy in some of our synthetic inversions below.

1 A key question for crustal-scale FWI then is whether it is possible to acquire data with  
2 adequate low-frequency content. For successful FWI, it is not the absolute amplitude at low  
3 frequency that is important, but rather the signal-to-ambient-noise ratio at particular  
4 frequencies. For deep-water hydrophones, there is no instrumental limit on low-frequency  
5 response, and no significant effect from the distant surface ghost. In the absence of noise  
6 generated locally by ocean-bottom currents, which is only problematic in limited areas, the  
7 deep-ocean is very quiet at low frequencies down to sub 1-Hz frequencies below which  
8 micro-seismic noise related to ocean swell begins to increase (Urick 1984). There is no  
9 major issue therefore in recording low-frequency hydrophone signals near the seabed in  
10 deep water provided only that we have a source that can generate them.

11 Fig. 2 shows data acquired as part of a 3D petroleum-industry ocean-bottom survey (Granli  
12 *et al.* 1999; Ratcliffe *et al.* 2012) using conventional airgun arrays as a source; note that this  
13 is not the same dataset as was shown in Fig. 1; the latter is from surface streamers. The  
14 left-hand panel in Fig. 2a shows an example of time-domain data generated by a single  
15 source recorded on a single ocean-bottom-hydrophone cable. Fig. 2b shows the same data  
16 windowed in time using a Gaussian window centred upon the early refracted arrivals. The  
17 data have been low-pass filtered at 8 Hz, and the RMS amplitude in each filtered trace has  
18 been normalised; amplitude normalisation was performed after windowing

19 The remaining four panels in Fig. 2 show 3D common-receiver gathers after transformation  
20 into the frequency domain. Each of the four panels shows the phase at a single frequency.  
21 The receiver is located at the centre of the circular features. Each coloured pixel in these  
22 plots corresponds to the location of a single source, and the horizontal white lines  
23 correspond to missing lines of sources that were not acquired. The upper figures correspond  
24 to the un-windowed time-domain data, and the lower figures correspond to the windowed  
25 data. In a one-dimensional velocity model, these plots would show concentric circles centred  
26 on the receiver position. Here, the velocity model is approximately one-dimensional; the  
27 deviation from circularity seen in the bottom right of the figures is produced by a low-velocity

gas cloud that we have previously imaged by applying FWI to these data (Ratcliffe *et al.* 2012; Warner *et al.* 2013a).

Spatially coherent structure on receiver gathers indicates source-generated signal. At 3 Hz, with or without windowing, the right-hand panels in Fig. 2 show that there is clearly a good ratio of source-generated signal to ambient noise. At 2 Hz, with no pre-processing, there is some coherent signal visible, but the signal-to-noise ratio is poor. However, as shown in the bottom panel at 2 Hz, simple windowing of the data onto the early arrivals dramatically improves both the coherency and the signal-to-noise ratio. For the early refracted arrivals, there is now low-frequency signal available that is more than adequate to begin a suitably designed FWI scheme. In a typical workflow, as the inversion proceeds, the frequency bandwidth is increased, and the tight windowing onto just early arrivals is relaxed.

The data shown in Fig. 2 were not acquired with low-frequencies in mind. A conventional petroleum-industry airgun array was towed at a depth of 6 m, and the array was tuned to provide a flat spectrum from about 10 to 80 Hz. During the acquisition, low-cut field filters were set to roll off below 3 Hz at 18 dB per octave. At 2 Hz therefore, we are working below the nominal cut-off frequency of the recording system. However, these filters reduce both the signal and the noise equally, and therefore do not affect the signal-to-noise ratio at low frequency since the inherent instrumental noise is very low. The field filters, the design of the airgun array, and especially the source ghost produced by the shallow tow-depth, all however reduce the absolute magnitude of the signals at low frequency; at 2 Hz, the available amplitude is about 50 dB below that available at 10 Hz. For FWI, these low absolute amplitudes are unimportant; provided that we have good signal-to-noise ratios at a particular frequency, then we can invert the data successfully at that frequency.

The data shown in Fig. 2 demonstrate that a shallow, conventional, airgun source, when combined with ocean-bottom hydrophone recording in a quiet environment, can routinely provide good quality data for FWI at frequencies down to 2 Hz. Brenders *et al.* (2012) report

1 that they were able to begin mono-frequency FWI at 1.7 Hz on a conventional commercial  
2 airgun dataset, and Vigh *et al.* (2011) started their inversion of wide-azimuth towed surface-  
3 streamer data from the Gulf of Mexico at 2.2 Hz. The major seismic contractors report that  
4 they are able to extract useable signals from airguns recorded by hydrophones in deep water  
5 "down to about 2 Hz" provided that there is no significant effect from receiver-side surface  
6 ghosts and that the low frequencies are not deliberately removed by inappropriate  
7 instrumental filters (personal communication, CGG, WesternGeco & PGS).

8 We note that the data in Fig. 2 were acquired in only about 75 m of water in the North Sea.  
9 Ambient noise in this shallow sea is likely to be much higher than in the deep ocean; wave  
10 noise is generated much closer to the receivers in shallow water, the coast line and  
11 associated breaking waves are not far distant, and the central North Sea is an active area for  
12 shipping and oil exploration with a wide range of cultural activities generating noise at the  
13 sea surface, in the water column, and on the seabed. With more specialised acquisition, a  
14 quieter recording environment, and more-sophisticated noise reduction during pre-  
15 processing, it seems reasonable to expect practical FWI to start at about half the  
16 frequency that is now routinely undertaken with standard systems operating in more-noisy  
17 shallow water, that is we expect to be able to operate at frequencies down to about 1 Hz.

18 Shah *et al.* (2012a) report a linear scheme in the frequency domain that uses the unwrapped  
19 phase to reduce the lowest frequency at which FWI can begin. Warner *et al.* (2013b)  
20 demonstrate a non-linear processing scheme in the time domain that can halve the lowest  
21 frequency usefully present in the field data prior to FWI. A number of recent developments  
22 also promise the ability to apply FWI directly and successfully to higher-frequency field data  
23 that are cycle skipped (Shah *et al.* 2012b; Biondi and Almomin, 2012; van Leeuwen and  
24 Herrmann, 2013). None of these new methods have yet proved themselves in routine  
25 production, but there are sufficiently many novel approaches appearing in this area that at  
26 least some of them seem likely to prove themselves capable of overcoming the problem of  
27 cycle skipping during FWI in the near future.

1 For air gun sources, which are currently the only practical and environmentally acceptable  
2 marine sources available for long-offset acquisition, there are two important limitations on  
3 low-frequency response – the source ghost and the fundamental bubble frequency (Lau *et al.*  
4 2007). The effects of the source ghost vary directly with source depth – the deeper the  
5 source the better the low-frequency response. The effects on the bubble are in the opposite  
6 direction – deeper sources have a reduced low-frequency response. The latter effect can be  
7 offset by increasing either the airgun volume or the airgun pressure. There are significant  
8 technical difficulties involved in increasing airgun pressures more than marginally, but it is  
9 relatively straightforward to increase gun volumes, either by using larger individual guns, or  
10 by clustering multiple guns so that their bubbles coalesce.

11 For the 3D inversions run below, we begin the inversion at frequencies no lower than 1 Hz.  
12 To obtain useful signals at 1 Hz using an acquisition system that is already able to provide  
13 adequate signals at 2 Hz, we would need to tow the airguns at around 14 m rather than 7 m,  
14 and to increase the total volume by about 5.5 times. The latter figure is because the bubble  
15 frequency scales inversely as the cube root of gun volume and scales proportionately to the  
16 gun depth to the power of five sixths (Ziolkowski, 2006). In practice this means using an  
17 array volume of around 17,000 cu ins. We have previously used array volumes of 9162 cu  
18 ins on a commercial seismic vessel to acquire deep data in the Gulf of Mexico (Morgan *et al.*  
19 1997), including wide-angle recordings on land and on the seabed at distances of over 200  
20 km (Christeson *et al.* 2001), and array volumes of 14,500 cu ins during a commercial survey  
21 on the UK continental shelf. We have also towed airguns at 15 m depth without any  
22 particular operational difficulty. Lau *et al.* (2007) report the successful use of a bubble-tuned  
23 array, that included 1000 cu ins individual airguns, towed at depths of 18 to 22 m below  
24 surface. This array, designed specifically for sub-basalt imaging, was able to generate  
25 signals at 1 Hz that were recorded on a sea-bottom hydrophone array at only 30 dB below  
26 the peak-amplitude signals generated at about 9 Hz – this is 15 dB above the 3 Hz signals  
27 that we used successfully to invert the data from Fig. 2 (Warner *et al.* 2013a).

28 The principal technical limitation on array volume is compressor capacity – however, FWI  
29 does not require the closely spaced sources that conventional high-resolution reflection  
30 profiling employs, so that the increased shot spacing during FWI acquisition allows the  
15

operation of very large airgun arrays using only conventional flow volumes from the compressors. There is therefore no great technical or commercial difficulty in running large airgun arrays, with volumes of up to about 20,000 cu ins at 14 m depth delivering signals down to about 1 Hz. Obtaining signals below about 1 Hz however is likely to prove to be much more challenging, but this does not appear to be necessary for the targets and models that we discuss below.

## CASE STUDIES

We have constructed three synthetic velocity models, using available geological and velocity data, that span the range of targets that are likely to be of interest within the crystalline crust and uppermost mantle. The first model is of the subsurface magma system beneath an active volcano in Montserrat. The second is a deep-water section from the Campos Basin, Brazil, across the transition from continental to oceanic crust. The third is a model of oceanic crust and upper mantle across the East Pacific Rise. In all three cases, conventional 3D reflection imaging is expected to be difficult or inadequate for a variety of reasons. We have run a suite of synthetic 3D FWI tests to explore which experimental geometries and inversion strategies are able to recover the fine-scale structure in these synthetic velocity models.

Although our 3D FWI codes have anisotropic, anelastic and elastic capabilities, here we use predominantly acoustic inversion since 3D elastic inversion is not yet well established within the petroleum industry. Our forward models were isotropic, had no anelastic attenuation, and maintained a fixed relationship between P-wave velocity and density. The majority of the forward modelling used an acoustic code, but in our final case study we also ran acoustic and elastic inversions applied to elastically modelled input data to explore the importance of the acoustic approximation in transmission FWI for crustal studies.

In the petroleum industry, FWI often incorporates anisotropy as an *a priori* model (Selwood *et al.* 2013; Warner *et al.* 2013a). Anisotropy adds a level of computational complexity to the inversion code, but it does not otherwise change the fundamentals of resolution, bandwidth, cycle skipping and fidelity that can be recovered in a synthetic study. In contrast, direct inversion for the anisotropy parameters themselves as part of FWI is still an area of active



1 research (Prioux *et al.* 2011), and is not yet a fully robust and routine procedure.

2 Full-elastic inversion of 3D field data is beginning to be practical (Guasch *et al.* 2012; Lu *et*  
3 *al.* 2013; Vigh *et al.*; 2013b), but this is still a computational task that is beyond the  
4 commercial budgets of most major oil companies for more than the smallest surveys. Elastic  
5 FWI requires a starting model for both P and S-wave velocity, and since the S-wave  
6 wavelength is shorter than that of the P-waves, the starting model for S-wave velocity must  
7 be correspondingly more accurate than the P-wave model by this ratio. In the absence of  
8 direct measurements in boreholes, it is often difficult in real datasets to obtain an S-wave  
9 starting model that is sufficiently accurate to begin useful full-elastic FWI without cycle  
10 skipping affecting the shear-wave portion of the record. In view of the high computational  
11 costs, and the genuine practical difficulties of obtaining the necessary S-wave starting model,  
12 we do not pursue elastic FWI in this paper beyond showing a single example. However we  
13 recognise, where it is feasible and affordable, that elastic FWI has significant potential and is,  
14 in principle, capable of providing information beyond that which a purely acoustic inversion  
15 can recover, and these additional constraints may have great value in helping to separate the  
16 effects of fluids, temperature and lithology

17 The only technically feasible and cost-effective way to acquire long-offset, multi-azimuth,  
18 crustal-scale seismic data in deep water is to use stand-alone ocean-bottom or water-column  
19 receivers. For acoustic FWI, we require only hydrophones, and these are much simpler and  
20 cheaper to install than are properly coupled ocean-bottom geophones. In marine field  
21 experiments, individual ocean-bottom receivers are expensive and are slow to deploy,  
22 whereas airgun sources are fast and cheap to operate. Consequently we have explored  
23 experimental designs that use very many airgun sources and a relatively small number of  
24 autonomous ocean-bottom hydrophones. One feature of three-dimensional transmission  
25 FWI, that is significant in this context, is that the lateral spatial resolution is less strongly  
26 dependant upon source and receiver separation in well designed experiments than it is in  
27 many other types of seismic experiment. In the experimental designs below, we take  
28 advantage of this, and show that we can resolve fine structure that is significantly smaller  
29 than the receiver spacing.

1 In each case study, we have constructed P-wave starting velocity models that are consistent  
2 with the spatial resolution that we expect to be able to obtain using wide-angle travel-time  
3 tomography (e.g. Morgan *et al.* 2011) and reflection tomography (e.g. Woodward *et al.*  
4 2008). In all our inversions, we have adopted a multi-scale method (e.g. Bunks *et al.* 1995;  
5 Sirgue & Pratt 2004), inverting from low to high frequencies, which helps to avoid local  
6 minima in the objective function and that also mitigates against cycle-skipping.

7 To avoid cycle-skipping, starting models should be able to reproduce the recorded wavefield  
8 to within half a cycle at the lowest inversion frequency. If the lowest frequency used during  
9 FWI is 1 Hz, then this requirement means that our travel-time tomography must be capable  
10 of matching travel times to better than 500 ms for the main arrivals. If we are using layer  
11 stripping during FWI, then this requirement need only be met by that portion of the data that  
12 is inverted initially, and then met subsequently by the next portion of data with respect to the  
13 already-recovered model. Crustal-scale travel-time tomography can normally be expected to  
14 fit field data to an accuracy of no worse than about 250 ms (Zelt, 2011) which means that  
15 practical crustal experiments need to acquire data only down to about 2 Hz in order to begin  
16 FWI in all but the most difficult and complex regions.

## 17 **Montserrat**

18 The Soufrière Hills Volcano, Montserrat, is part of the Lesser Antilles island chain in the  
19 Caribbean. The volcano has been active since 1995 and early eruptions destroyed the  
20 capital city of Plymouth. A wealth of geophysical and geochemical data have been acquired  
21 since the start of the eruptions, and these data have been used to understand better the  
22 storage and transport of magma to surface (e.g. Zellmer *et al.* 2003; Mattioli *et al.* 2010;  
23 Voight *et al.* 2010). In one model, the crustal magma system is argued to be composed of  
24 two distinct magma chambers separated by a conduit dyke (Elsworth *et al.* 2008; Foroozan  
25 *et al.* 2010). These chambers would be difficult to image using conventional seismic  
26 reflection data, because the target lies directly beneath the active volcano where the terrain  
27 is hazardous and inaccessible, and because the shallow chamber will tend to obscure the  
28 deeper one for near-vertical ray paths.

1 In 2007, wide-angle seismic data were acquired across the volcano in the SEA CALIPSO  
2 experiment (Voight *et al.* 2010), and inverted using first-arrival 3D travel-time tomography. A  
3 low-velocity zone was observed at depths of 5-8 km below the Soufrière Hills Volcano, Fig. 3,  
4 and interpreted to represent a shallow magma chamber (Paulatto *et al.* 2012). The  
5 resolution of the chamber using travel-time tomography is however restricted to a Fresnel  
6 zone (3-4 km in this case), and the maximum depth of penetration was limited as the  
7 experiment had a maximum source-receiver offset of about 50 km. The magma chambers  
8 are an ideal target for a wide-angle seismic survey combined with 3D FWI since the  
9 amplitude of the velocity anomaly is large, and Montserrat island is sufficiently small, that  
10 imaging would not be compromised by an acquisition geometry involving only offshore  
11 seismic sources.

12 The 3D travel-time tomographic velocity model, Fig. 3, obtained by Paulatto *et al.* (2012) was  
13 used to construct true, Fig. 4a, and starting velocity models for the inversions. The models  
14 have been extended laterally and deepened in accordance with expectations for whole-  
15 crustal velocities in this region (Christeson *et al.* 2008). In these models, the grid spacing is  
16 200 m, and the models are 100 km long, 15 km wide and 20 km deep. The true model has  
17 two spherical magma chambers with radii of 1.75 km and velocities that are 1200 m/s lower  
18 than the background velocity, in accordance with the models of Paulatto *et al.* (2012). The  
19 chambers are located at depths of 6 and 11 km, as suggested by Elsworth *et al.* (2008). The  
20 starting model does not contain the magma chambers.

21 The true velocity model was used to generate 3D synthetic seismic data, using a range of  
22 different experimental geometries, assuming sources would be fired using airguns, and  
23 receivers placed on Montserrat and on the ocean floor. Recovering a reasonably extensive  
24 model across the volcano within the lower crust requires an inline survey length of around  
25 100 km. We have kept the cross-line extent of the survey relatively restricted at 15 km to  
26 keep the acquisition costs of a field survey realistic, but still allow for multi-azimuthal  
27 sampling of the magma chambers. The synthetic data were inverted using FWI to determine  
28 how well the structure of the magma chambers below Montserrat could be recovered. One  
29 of the results from these 3D inversions is shown Figs 4b and 5.

FWI clearly performs well in recovering the dimensions, amplitude, and location of the two magma chambers. For this inversion, we used 1500 airgun sources distributed along twelve shot lines with a shot spacing of 750 m in both directions, and 90 receivers in total spaced every 3 km along three receiver lines which were 2.5 km apart; thus the receivers only span the central 7.5 km of the model. We ran 30 iterations, 6 iterations at each of 5 frequencies, starting at 1 Hz and extending to 1.8 Hz. A 200-m grid spacing, along with a minimum model velocity of  $1500 \text{ m s}^{-1}$ , restricts the maximum inversion frequency to 1.8 Hz, because of the requirement for a minimum of four grid points per seismic wavelength by our finite-difference modelling software. As the resolution of FWI is around half the seismic wavelength, this means, for this synthetic experiment, that the resolution across the two magma chambers should be between 1000 and 1500 m. This is consistent with the inverted velocity model shown in Figs 4b and 5 in that we are able to recover two separate magma chambers, but the sides of the magma chambers are smoother than in the true model. Fig. 5 also shows the iterative improvement in the velocity model.

Finally, we ran checkerboard tests to explore resolution across the model, and to determine whether the experimental geometry would allow us to detect features outside the predicted location of the two magma chambers. A checkerboard of  $\pm 100 \text{ m s}^{-1}$  was added to the background velocity model; a vertical slice is shown in Fig. 6a. The velocity model was re-sampled to a 100 m grid spacing in order to increase the maximum inversion frequency to 3.75 Hz. A checkerboard of 1000 x 1000 m horizontally, and 900 m vertically was tested since this corresponds to about half the seismic wavelength for mid-crustal velocities of around  $6700 \text{ m s}^{-1}$ , and we expect this to be resolvable. The starting model was the background velocity model without the checkerboard. In total, 10 iterations were performed at each of 4 frequencies: 2.9, 3.1, 3.3 and 3.75 Hz. Having previously recovered the background model, we are able to begin the inversion at 2.9 Hz since the wavefields through the starting and true models are now not cycle-skipped at this frequency.

Vertical slices through the true and recovered checkerboards are shown in Figs 6b and c, respectively; horizontal slices are shown in Figs 6d and e. Within the central region of the model, the magnitude of the velocity anomaly ( $100 \text{ m s}^{-1}$ ) within the upper checkerboard is fully recovered, while the amplitude of the velocity anomaly within the lower checkerboard,

1 where full-azimuthal coverage is reduced, is recovered to only about 85% of its true value. In  
2 the centre of the model where there is good azimuthal coverage, FWI is able to resolve the  
3 individual checkers in all three directions confirming that the practically achievable spatial  
4 resolution is indeed equal to the theoretical value of around half the seismic wavelength.  
5 Note that in this experiment, the receiver separation is about three times larger than the  
6 achieved spatial resolution, such that very large numbers of ocean-bottom hydrophones will  
7 not be required in field experiments in order to resolve the model.

8 As FWI continues to advance, elastic inversion for S-wave velocity (e.g. Guasch *et al.* 2012;  
9 Lu *et al.* 2013), and anelastic inversion for attenuation (e.g. Bai & Yingst 2013; Prieux *et al.*  
10 2013), are expected to become increasingly practical. Although the former in particular will  
11 always remain more expensive than acoustic inversion in 3D, inversion for S-wave velocity  
12 and attenuation should be able to distinguish more readily than can P-wave velocity alone  
13 between partially molten and high-temperature zones, and identify magma pathways  
14 throughout the crust, as well as determine whether a deep crustal hot zone (similar to that  
15 proposed by e.g. Solano *et al.* 2012) exists beneath the Soufrière Hills volcano. All of these  
16 would represent major improvements in our understanding of active volcanoes and in our  
17 ability to predict their behaviour.

## 18 **Campos Basin, Brazil**

19 The Campos Basin is a Brazilian coastal sedimentary basin close to Rio de Janeiro, where  
20 exploration for hydrocarbons has been ongoing for over 35 years (Fraga *et al.* 2003). The  
21 search for oil has gradually moved to deeper water (Greenhalgh *et al.* 2011), and one of the  
22 targets is the sag-basin sediment, located within the transition zone between continental and  
23 oceanic crust, Fig. 7. Salt bodies of variable thickness lie above these sediments.  
24 Conventional reflection data have often failed to produce high-quality images of reflectors  
25 within the sag-basin sediments, to locate accurately top basement or the boundary between  
26 stretched continental and oceanic crust, and to determine crustal thickness. This not only  
27 means that potential reservoirs are difficult to identify, but also that maturation histories are  
28 poorly constrained (White *et al.* 2003).

1 Although whole-crustal velocity data are limited for the Campos Basin, wide-angle refraction  
2 data have been acquired across its conjugate margin in offshore Angola (Contrucci *et al.*  
3 2004). In the refraction model of Contrucci *et al.* (2004) there are anomalous velocities of  
4  $6800\text{--}8000\text{ m s}^{-1}$  in the upper mantle beneath the Moho, which are postulated to exist also in  
5 the mantle beneath the Campos basin (Unterneh *et al.* 2010, fig. 3a). These velocities may  
6 represent serpentinised mantle and/or a zone of magmatic underplating (Mohriak *et al.* 1990;  
7 Lavier & Manatschal 2006).

8 A geological model of the Campos basin and continent-ocean transition was constructed  
9 using the model of Unterneh *et al.* (2010) shown in Fig. 7; the refraction velocity model of  
10 Contrucci *et al.* (2004) was used to assign velocities to each stratigraphic unit. The resulting  
11 synthetic velocity model is shown in Fig. 8a. The water depth varies between 2200 and 2800  
12 m. The post-rift reflective sediments have velocities of between  $1900\text{ and }3200\text{ m s}^{-1}$  and  
13 the sag-basin sediments have velocities in the range  $4800\text{--}5600\text{ m s}^{-1}$ . Two thin (300-600  
14 m) antiformal/synformal structures have been added with velocities of  $\pm 500\text{ m s}^{-1}$  above and  
15 below the background velocity; these features were included to represent generic structure of  
16 similar scale to that of interest for regional hydrocarbon exploration in these sediments.  
17 Between the two sedimentary units are laterally variable salt bodies with a velocity of  $4500\text{ m s}^{-1}$ ,  
18 which have a geometry that is consistent with the seismic reflection data shown in  
19 Unterneh *et al.* (2010). The sediments and salt lie above a hyper-extended continental  
20 crust. Although the exact location of the continent-ocean boundary (COB) is unclear from  
21 current data, in the synthetic model, Fig. 8a, the boundary is represented by a sharp  
22 transition to normal oceanic crustal velocities of  $6500\text{--}6800\text{ m s}^{-1}$ . Layering has been added  
23 in the anomalous mantle zone to represent sill intrusions.

24 The starting model, Fig. 8b, has no layering in the uppermost sediments and anomalous  
25 lower crust/mantle, or antiformal/synformal structures in the sag-basin sediments. Beneath  
26 the salt, the velocities have been smoothed laterally and vertically, so that they have a similar  
27 resolution to the refraction model of Contrucci *et al.* (2004) for the conjugate margin, offshore  
28 Angola. Velocities within and above the salt are less smooth since conventional velocity  
29 analysis and reflection tomography are able to recover velocities accurately within these  
30 sediments including the structure of the top of the salt.

1 This initial 2D velocity model was extended into 3D with no lateral change in velocity across  
2 the width of the model. This velocity model was used to generate 3D synthetic data, using a  
3 range of different experimental geometries, assuming near-surface airgun sources and  
4 ocean-bottom receivers. These synthetic data were inverted using 3D FWI to determine  
5 whether they could recover structure within the sag-basin sediments, the sharp continental-  
6 oceanic boundary, and the layering in the anomalous mantle. These targets are important  
7 for identifying potential hydrocarbon reservoirs and for understanding maturation history.  
8 Results from two of these inversions are shown in Figs 8c and 8d.

9 For the inversions, the 3D velocity models were 100 km long, 15 km wide and 20 km deep,  
10 and the grid spacing was 120 m. For the inversion shown in Fig. 8c, there were 6426  
11 sources in total distributed along 27 shot lines with a shot spacing of 400 m in both  
12 directions, and 441 receivers located along 7 lines with a receiver spacing of 1.5 km in both  
13 directions. Sources were placed close to the surface and receivers close to the sea-bottom.  
14 The vertical slice in Fig. 8c is parallel to the central receiver line. We windowed the raw  
15 seismic data in time to select only the refracted arrivals, and used a layer-stripping approach  
16 to overcome cycle skipping in the starting model. The model updates were restricted to  
17 occur in the top 10 km of the model, and 10 iterations were run at frequencies of 1.0, 1.3,  
18 1.7, 2.2, 2.5 and 2.9 Hz. Model updates were then allowed across the entire depth of the  
19 model, and the inversion re-started with the same number of iterations at each frequency.

20 In Fig. 8c, the antiformal/synformal structures and continental-ocean boundary are well  
21 resolved. The lower crustal/mantle layering is emerging, but is not quite resolvable at the low  
22 frequencies that we are using here. We used a large number of receivers in this study since  
23 it is a survey that is most likely in practice to be undertaken by the petroleum industry which  
24 has access to large numbers of ocean-bottom receivers. In Fig. 8d we also show the results  
25 of running an inversion with only 90 receivers spaced 3 km apart and located along three  
26 lines that were 2.5 km apart; this acquisition geometry is similar to that used for Montserrat.  
27 The other inversion parameters were identical except that 20 iterations were run at 2.2, 2.5  
28 and 2.9 Hz. The inversion using only 90 sources is still able to recover the main features of  
29 the structure, though it is slightly noisier and the thick layer in the lower crust is less well-  
30 resolved than can be obtained using the larger survey. The noise in the velocity model in  
23

Fig. 8 is incoherently speckled across the entire model. This characteristic is fairly common in FWI (e.g. Brenders & Pratt 2007), and its consistency of appearance across the model is helpful in aiding interpreters to distinguish between residual noise and real geological structure.

A frequency of 2.9 Hz suggests a maximum resolution of about 850 m in the sag-basin sediments, and 1100-1300 m across the continental-ocean transition and lower crust. In Fig. 8, the sag-basin structures are easily detectable even though they are only 500 m thick. The thickness and velocity of these bodies is close to those in the true model; the inset in Fig. 8d shows a virtual borehole through the true and recovered models, with the starting model subtracted from each. All the main velocity anomalies in the sediments are recovered well; the results suggest that more iterations at higher frequencies would improve the resolution further.

To understand fully the results in Fig. 8, and especially to understand our ability to detect clearly features that are below the nominal half-wavelength resolution, we must differentiate between resolution and detectability. Resolution concerns the ability to distinguish and separate two discrete features whereas detectability concerns the ability merely to detect the presence of a feature in an otherwise largely featureless background. For the latter, FWI is able to detect individual features that have scale lengths of only about a tenth of a wavelength in thickness provided that they have substantial extent in at least one other direction – that is, we can detect thin layers and thin lineations. Achieving this however requires a finer mesh than would normally be employed during FWI, and so the computational cost is considerable. For the maximum frequencies that we are using here, we would expect to be able to resolve, and separate, equi-dimensional features of about 850 m in extent or larger, but to be able to detect laminar and linear features that are around 170 m in thickness. For the correspondingly higher frequencies that we would invert in field data, the resolution and detectability improve in direct proportion to the shortest seismic wavelength used during the inversion.

Finally, we ran a checkerboard test to explore further the resolution within the sag-basin sediments and anomalous mantle. A checkerboard of  $\pm 100 \text{ m s}^{-1}$  was added to the starting



velocity model, Fig. 8b; a vertical slice is shown in Fig. 9a. We used the velocity model sampled on a 120 m grid spacing, which restricts the maximum inversion frequency to 3.1 Hz. We chose a checkerboard of 1200 x 1200 x 1200 m as this corresponds to about half a seismic wavelength for mantle velocities of 8000 m s<sup>-1</sup> and an inversion frequency of 3.1 Hz, but the uppermost checkerboard within the sediments was reduced to 800 m in height as this corresponds to the theoretical resolution of FWI in this region. The starting model is the background velocity model without the checkerboard. In total, 20 iterations were performed at each of 3 frequencies: 2.9, 3.0 and 3.1 Hz. We are able here to begin the inversion at 2.9 Hz because the wavefields through the starting and true models are not cycle-skipped. Vertical slices through the true and recovered checkerboards are shown in Figs 9b and c, respectively, and horizontal slices in Figs 9d and e. The upper checkerboard is recovered well across the entire model, whilst the lower checkerboard is recovered well near the model centre but less well elsewhere. This is presumably because the central region is better sampled by multiple wavefields.

## **East Pacific Rise**

The final case study is across the East Pacific Rise (EPR). A wealth of seismic and other geophysical data have been acquired across the EPR at various locations which, together with geological and geochemical studies of ophiolites, have provided a good understanding of the large-scale processes involved in the formation of oceanic lithosphere at fast-spreading mid-ocean ridges (e.g. Detrick *et al.* 1987; Mutter *et al.* 1995; Boudier *et al.* 1996; Korenaga & Kelemen, 1998; Dunn *et al.* 2000; Singh *et al.* 2006).

Understanding of the accretion of lower oceanic crust however remains unclear, with two end-member models, Fig. 10, being advocated: (a) a gabbro glacier model (e.g. Henstock *et al.* 1993; Phipps Morgan and Chen, 1993), and (b) a multiple sheeted-sill model (e.g. Korenaga & Keleman, 1998; MacLeod & Yaoancq, 2000). Distinguishing between these and a host of intermediate models is problematic because, with a careful selection of parameters, the proposed models are all consistent with the available data (MacLennan *et al.* 2004). One issue with current 3D velocity models of the lower crust across the EPR is that they have been obtained using travel-time tomography (e.g. Dunn *et al.* 2000), which has a resolution

1 of a few kilometres. Here we investigate whether 3D FWI is able to recover a high-resolution  
2 velocity model of the lower oceanic crust and uppermost mantle, which would help  
3 distinguish between competing models of crustal accretion.

4 We have constructed a simple synthetic 3D velocity model of the East Pacific Rise based  
5 upon the thermal model of Henstock *et al.* (1993), Fig. 11a, and added a 1000 m  
6 checkerboard in the shallow crust, deep crust, and immediately below the Moho, in which the  
7 velocity varies by  $\pm 100 \text{ m s}^{-1}$  relative to the background, Fig. 11b. We use a simple  
8 checkerboard here because there is no broadly agreed model for the true small-scale  
9 structure that should be expected. The shallow checkerboards are not in this case included  
10 principally as targets that we seek to recover; they serve rather as heterogeneities beneath  
11 which we seek to image deeper structure. Specifically we demonstrate how well we can  
12 recover P-wave velocity on a horizontal slice immediately beneath the Moho, Fig. 12a. The  
13 results that we obtain at this level will contain a superposition of all the velocity errors  
14 throughout the crustal model as well as responding directly to heterogeneity within the  
15 mantle at this depth, and so they provide a simple means of summarising the accuracy of the  
16 whole crustal model.

17 We have used this model to generate and invert both acoustic and full-elastic synthetic data.  
18 The model and inverted data included a free surface so that the data contain both ghosts and  
19 free-surface multiples. The model measured  $40 \times 32 \times 12 \text{ km}$ . We used 8000 airgun shots  
20 fired at an interval of 360 m inline and cross line, and just 60 ocean-bottom hydrophones  
21 deployed at 3600 m spacing inline and crossline. For most experiments, the hydrophones  
22 occupied a central portion of the model that measured about  $26 \times 15 \text{ km}$ , shown by the  
23 yellow receivers in Fig. 12b. Assuming a source vessel steaming at around 5 knots, towing  
24 only a single airgun array and no surface streamer, the 8000 sources would represent about  
25 13 days of continuous acquisition in the field.

26 Fig. 13 shows a record from an ocean-bottom hydrophone recording a line of sources  
27 perpendicular to the strike of the EPR. In order to improve the clarity of this figure, and for  
28 this figure only, the sources were spaced at 60 m intervals in-line; this is six times more  
29 dense than the source spacing used for the inversions. Fig. 13a shows the raw data

1 modelled acoustically including surface-related multiples. We stop both modelling and  
2 inversion at 10 s, and this allows time for only the first surface-multiple to appear.

3 Fig. 14a shows the results of inverting these data using all 8000 sources and all 60  
4 hydrophones, starting from 2.4 Hz, stepping up to 6.6 Hz in seven stages, using 42 iterations  
5 in total and six iterations per frequency. The data were truncated at 10 s, but are not  
6 otherwise muted in time. The data are noise-free, and the starting model used the  
7 background model of the EPR without the checkerboard. Later, we show results obtained  
8 using less-accurate starting models, using elastic data, adding noise and windowing in time.  
9 Fig. 14a therefore provides a benchmark result showing what can be achieved using perfect  
10 data and a good starting model.

11 Clearly, under these ideal circumstances, FWI can recover short-wavelength heterogeneities  
12 in the upper mantle with high fidelity. The result is not perfect – we are using finite-  
13 bandwidth data, that has a minimum wavelength of about 1100 m at the depth of this image,  
14 to probe structures that have sharp boundaries at a much shorter scale length than this.  
15 Consequently the recovered checkerboard is not as sharp as the true model, and it does not  
16 fully capture the absolute magnitude of the anomalies – it represents a low-pass filtered  
17 version of the true model with a cut-off wavelength of about half the minimum seismic  
18 wavelength, in this case about 550 m. In order to recover shorter wavelength anomalies, we  
19 would need to operate at correspondingly higher maximum frequencies.

20 In practice, when inverting deep-water field data, we almost always mute the later arrivals,  
21 typically removing all the free-surface multiples, any double-converted shear-waves that are  
22 visible on the hydrophone data, and often most or all near-normal-incidence reflections. Fig.  
23 13b shows data that have been low-pass filtered to match the bandwidth used during FWI,  
24 and then muted to retain only the early transmitted P-wave arrivals; the record is shown to  
25 the full offset range used during inversion. The results of inverting these muted data are  
26 shown in Fig. 14b. Superficially this result looks similar to Fig. 14a, although it is  
27 quantitatively not quite such a good match to the true model when averaged over the entire  
28 model. This comparison illustrates two important features of FWI as it is used here: it clearly  
29 is not significantly aided or driven by short-offset reflections since these were not used to

1 obtain Fig. 14b, and transmission FWI remains robust when long-period surface-related  
2 multiples are included in the inversion window as they were to obtain Fig. 14a.

3 The results of FWI shown in Figs 14a and 14b are noise free; there is no noise added to the  
4 synthetics, and the physics used for the forward modelling and for the inversion is identical.  
5 For field data, both of these are unreasonable assumptions. Fig. 14c shows how FWI  
6 performs when spatially uncorrelated noise is added to the synthetic data. Here the signal-  
7 to-noise ratio was 2:1 by which we mean that the RMS value of the clean signal was twice  
8 the RMS value of the noise averaged over the 10s window that we use in the inversion. The  
9 data were muted as for Fig. 14b prior to inversion. The result in Fig. 14c is similar to the  
10 result in 14b but it is now itself somewhat noisy. The effect of the random noise is least in  
11 the centre of the image where the azimuthal coverage and density of data are greatest, and it  
12 is worst around the edges of the model where the coverage is incomplete. FWI is  
13 remarkably robust against incoherent noise; this is principally because it involves implicitly  
14 significant mixing between different portions of the data, and because there is typically no  
15 earth model in deep water that can generate data that are spatially incoherent over short  
16 sub-wavelength distances so that the noise cannot easily become incorporated into the  
17 model.

18 In Figs 14 a-c, the ocean-bottom hydrophones were uniformly and widely distributed across  
19 the model as shown by the yellow receivers in Fig. 12b. However, in many field experiments,  
20 this will not provide an optimal practical acquisition geometry given a limited total number of  
21 hydrophones, limited time to deploy and recover them, and an intent to use a single  
22 experiment to address multiple targets at different depths and with different resolutions. Fig.  
23 14d therefore explores one possible alternative geometry for the hydrophones. For this  
24 inversion, the 60 available hydrophones were concentrated over a reduced area occupying  
25 the left portion of the model and extending only a short distance across the axis of the EPR  
26 as shown by the green receivers in Fig. 12b

27 Fig. 14d shows that the resolution and fidelity of the deep FWI image is marginally improved  
28 relative to Fig. 14a in the region where the hydrophones are concentrated, but its ability to  
29 fully capture the amplitude of the anomalies is reduced over that portion of the model where

1 there are no hydrophones. Two conclusions can be reached from this comparison. Firstly,  
2 three-dimensional FWI is able to capture structure in the subsurface that has a wavelength  
3 that is several times shorter than the source or receiver separation provided that the model is  
4 well covered by many crossing wavefields so that, in a marine experiment where sources are  
5 cheap, rather few ocean-bottom receivers can be employed. This contrasts with travel-time  
6 tomography where the spatial resolution can be compromised by the source or receiver  
7 spacing, whichever is the largest. Secondly, FWI can recover fine details of the subsurface  
8 in portions of the model where there are only sources and no receivers at all, again provided  
9 that there are many independent wavefields sampling the area. This characteristic means  
10 that the size of the recovered model can be significantly larger than the acquisition footprint  
11 of the receivers.

12 Fig. 14 has shown that transmission FWI is robust against random noise, against inclusion of  
13 surface multiples, and against wide or irregular receiver spacing, and does not require or  
14 gain particular advantage from short-offset reflections. All these models though have used a  
15 starting model that is close to the true model, lacking only the checkerboard. Fig. 15  
16 explores the robustness of FWI to a less-accurate starting model.

17 To explore the importance of the starting model, we used starting models that were  
18 systematically incorrect – that is, the entire model below the seabed was either consistently  
19 too fast or too slow. Fig. 15 shows results for starting models that are fast; results from slow  
20 models are comparable. We show two scenarios; one where the starting model predicts  
21 arrival times for transmitted arrivals that are 200 ms early at 10 s travel time, and one where  
22 this error increases to 400 ms. The percentage error in the start model in these tests, before  
23 addition of the checkerboard, was everywhere the same below the seabed. In the 400 ms  
24 start model, the initial systematic velocity error in the uppermost mantle, where we present  
25 Fig. 15, was about 300 m/s outside the checkerboard, and ranged from 200 to 400 m/s within  
26 the checkerboard. Our experience of inverting travel times for field data across structures  
27 analogous to the one we explore here suggests that it is normally possible to build a travel-  
28 time model that is accurate to within  $\pm 200$  ms at 10 s travel time, and that it is always  
29 possible to match the travel time to better than  $\pm 400$  ms at 10 s given the reasonable signal-  
30 to-noise ratios that are seen in well-designed experiments using large airgun arrays recorded

29

on deep-water hydrophones.

We have run these inversions starting at 2.4 Hz and starting at 1 Hz. At 1 Hz, the starting model should not be cycle skipped at all for the 200 ms model. At 2.4 Hz, the 200 ms model is at the limit where some arrivals in particular directions through the checkerboard may be cycle skipped, but the majority of the data will not. In contrast, at 2.4 Hz, the 400 ms model will be badly cycle skipped at longer offsets and later travel times. At 1 Hz, the 400 ms model has some arrivals that are cycle skipped, but most are not. At 1 Hz, the checkerboard does not appear predominantly to the wavefield as heterogeneous, rather it appears to be anisotropic where, for example, the velocity in a horizontal plane parallel to the checkerboard is different to that in the diagonal direction. Note however that we are not here running anisotropic forward models or inverting for anisotropy; the apparent anisotropy is purely an effect of the organised heterogeneity, and FWI will have difficulty in capturing this when the incident seismic wavelength is large.

Fig. 15 shows that the inversion captures the checkerboard, that it recovers the true background model over much of the area, but that it does not significantly modify the starting model at the extreme left and right of the model where there is little or no data coverage. In these peripheral areas, few sources and few receivers contribute any energy to the model at this depth, and the limited energy that is recorded travels all in approximately the same direction.

Within the area for which there is reasonable data coverage, the checkerboard is recovered. For the 200 ms start model (Fig. 15 a & c), the background velocity is recovered correctly across all of the model away from the periphery, and the peripheral region is smaller for the 1 Hz FWI than for the 2.4 Hz FWI. At both frequencies, the recovered checkerboard is somewhat noisy, and its absolute amplitudes show a systematic variation from the centre to the edges of the checkerboard as the data coverage decreases. This systematic variation appears to be related to accumulated errors in the crustal section above this level; there is a bias towards lower checkerboard velocities in those portions of the model that underlie regions of lower velocity in the crust. Notwithstanding this, the quantitative match to the true model is reasonably close, and the structure and the location of individual elements is well

1 recovered. Surprisingly, the absolute velocities in the checkerboard at this level are better  
2 recovered by the 2.4 Hz result than by 1 Hz. We do not see this behaviour in the results  
3 recovered within the crust, and we do not have a complete and quantitative explanation for it.  
4 It seems likely that this anomalous behaviour is related to the apparent anisotropy that  
5 occurs at very low frequencies within this artificially regular model, and that the 1 Hz  
6 inversions do not deal with this properly, producing artefacts that the later higher frequencies  
7 cannot fully compensate.

8 For the 400 ms start model (Fig. 15 b & d), a similar pattern can be seen except that the  
9 background model is now no longer properly recovered when starting FWI at 2.4 Hz. This is  
10 not surprising given that these data are significantly cycle skipped in this start model.  
11 Interestingly, although the result is quantitatively wrong at 2.4 Hz, the geometry and the local  
12 contrast within the checkerboard region is well recovered. This is a common feature of FWI  
13 – even though it nominally fails when the input data are cycle skipped, it can still often  
14 recover the short-wavelength structure approximately correctly albeit superimposed upon an  
15 incorrect longer-wavelength model.

16 At 400 ms, starting at 1 Hz, the background model is well recovered, and is quantitatively  
17 correct, over most of the region where there is significant data coverage. This region is  
18 smaller than the corresponding region obtained when the initial error is only 200 ms. The  
19 checkerboard is well recovered, both structurally and quantitatively, but there is residual  
20 noise in the result that is higher than at 200 ms.

21 From these, and from similar tests run with low-velocity starting models, we conclude that,  
22 given the expected errors in starting models, beginning inversion on field data at 2.4 Hz is  
23 likely to be just adequate in order to recover both the short and long wavelengths in a model  
24 similar to this. If the errors in the starting model are larger than normal, then we will require  
25 lower frequencies in the field data. Beginning the inversion at 1 Hz appears to be adequate  
26 for the largest reasonable errors that are likely to appear in travel-time models. It is always  
27 easier to recover the fine structure at depth, even when using rather poor starting models,  
28 than it is to recover a model that is quantitatively exact.

29 Thus far, we have looked only at acoustic inversions performed using acoustic forward data.  
31

Fig. 16 shows FWI results obtained using elastically modelled forward data. Fig. 13c shows the same common-receiver record as is shown in Fig. 13a, but now it has been modelled using a full elastic code. Fig. 13d shows the muted elastic record corresponding to Fig. 13b. In this model, the water layer is acoustic, but the model below the seabed is elastic with a fixed  $V_p/V_s$  ratio of 1.73. Sources and receivers were located within the water layer, and so they do not generate or record shear-waves directly. The model used here has a hard water-bottom since there is no sedimentary cover on the East Pacific Rise; consequently P-to-S conversion is more effective at the seabed in this model than it is in almost any other deep-water environment so that acoustic-elastic differences are maximised in this example. Indeed, we have never seen shear-waves in field data in any environment on marine hydrophones, generated by airguns, that are as strong as those shown here.

The principal difference between the acoustic (Fig. 13a) and elastic (Fig. 13c) records, are the double-converted shear-wave transmitted arrivals that appear behind the faster P-waves. The generation of these shear-waves at the seabed extracts energy from the P-waves, and this therefore also causes amplitude differences between the transmitted P-waves seen on both records. The variation of amplitude with angle for reflected phases, especially as they approach and pass the critical angle, also varies between acoustic and elastic models. In this model, this is most apparent where it affects the wide-angle reflection from the Moho; wide-angle acoustic PmP reflections are consistently higher in amplitude than are their elastic counterparts. These various amplitude variations in turn affect the resulting interference patterns between different arrivals, and so they affect the resulting waveforms.

Comparison of Figs 13b and 13d shows the differences between the acoustic and elastic records within the window and the bandwidth that we retain for FWI. For acoustic FWI applied to field data, we record elastic data with the characteristics of Fig. 13d, and we invert these by modelling acoustic data with the characteristics of Fig. 13b. Since these two datasets are not dissimilar, it is unsurprising that acoustic FWI of elastic field data is able to recover an accurate P-wave velocity model when it is used as we describe here. In order for acoustic inversion of elastic data to be effective, we do not require that acoustic and elastic records from the same model be identical. Rather, we only require the weaker condition that acoustic data that are most similar to the elastic data should correspond to an acoustic



1 model that is close to the true P-wave model. This hypothesis is supported by both synthetic  
2 tests (e.g. Warner *et al.* 2012 and this paper) and by the application of acoustic FWI to field  
3 datasets that produce acoustic-velocity models that correctly migrate reflection data (e.g.  
4 Sirgue *et al.* 2010; Ratcliffe *et al.* 2012), that match direct measurements of P-wave velocity  
5 made in boreholes (e.g. Lazaratos *et al.* 2011; Warner *et al.* 2013a), and that correctly  
6 predict elastic field data when these are subsequently modelled elastically using the  
7 recovered acoustic velocity model as the basis for the elastic modelling (Virieux & Operto  
8 2009).

9 Fig. 16a shows the result of modelling data elastically, as in Fig. 13c, windowing the data as  
10 in Fig. 13d, and inverting the result acoustically. The acoustic FWI is able to recover the  
11 checkerboard, the result is quantitatively correct in the central third of the model where we  
12 have good data coverage, and there are no systematic artefacts or biases introduced in  
13 either the background model or within the checkerboard. The result is somewhat noisy, and  
14 it is not as well recovered as is a pure acoustic result in those portions of the model that have  
15 less than ideal data coverage. The result in Fig. 16a shows that acoustic inversion of full-  
16 elastic data is robust, and that transmission FWI is robust against at least some forms of  
17 coherent noise since we can regard the difference between acoustic and elastic  
18 seismograms as a form of source-correlated coherent noise.

19 Fig. 16b shows a result of applying elastic FWI to elastic forward data. If we do this using the  
20 correct S-wave model to invert for a P-wave model, something that we are unable to do in  
21 practice with field data, then the result is similar to the acoustic benchmark shown in Fig.  
22 14a. However, if we invert the hydrophone data elastically using an incorrect S-wave model,  
23 which is a more reasonable assumption for field data, then the resulting P-wave model is  
24 qualitatively similar to the result obtained by inverting elastic data using an acoustic  
25 algorithm, Fig. 16b. In this example, in the forward data, the checkerboard is present only in  
26 the P-wave model. During the inversion however, a fixed relationship is maintained  
27 everywhere between  $V_p$  and  $V_s$ . That relationship is correct outside the checkerboard, but it  
28 is not correct within it since the checkerboard is only present within the P-wave model.  
29 Consequently the P-wave model that is recovered by elastic FWI is unsurprisingly not  
30 quantitatively correct. If instead, we invert independently for  $V_p$  and  $V_s$  using these  
33

hydrophone data, then the result becomes worse since the observed data do not strongly constrain the short-wavelength shear-wave velocity model. In order to learn significantly more about the shear-wave model in this experiment, we would need to employ multi-component geophones deployed on the seabed.

## DISCUSSION

Our synthetic tests for all three case studies indicate that 3D FWI of wide-angle, multi-azimuthal data can be used to recover deep fine-scale sub-sedimentary velocity structures of interest that are unlikely to be resolved by any other technique. The minimum experimental requirement is that the wavefields sample the subsurface across a sufficient range of azimuths, which means that surveys can be long and moderately narrow – as they were for the Montserrat and Brazil case studies. The costs of such surveys are likely to be reasonable since they can use a relatively small number of ocean-bottom hydrophones and a dense grid of airgun sources. This is because the resolution, in multi-azimuth 3D transmission FWI, is controlled by the shortest inverted seismic wavelength, and to a lesser degree by the source or receiver spacing, whichever is the smallest. In our synthetic tests with few receivers, we found that we could obtain the expected resolution of half a wavelength, provided that this was larger than about half the source spacing in both directions, and that it was largely independent of the receiver spacing. Note that FWI explicitly includes surface ghosts and surface multiples into the forward wavefield during inversion. Consequently, there is no requirement for multi-component receivers in order to separate up and down-going wavefields, and hydrophones alone are adequate for acoustic inversions. This means that there is no necessity to couple geophones to the seabed which dramatically simplifies the design and deployment of the ocean-bottom instrumentation, with a corresponding reduction in both capital and operational cost.

For field data a number of issues will make such experiments and inversions more difficult than is suggested by our synthetic tests. These include the requirement to know accurately the positions of receivers on the ocean bottom, to have a good model of velocity in the water column, to have an inversion strategy that can deal effectively with attenuation, anisotropy and elastic effects where we seek to use these in the subsequent interpretation, and

1 especially to have low frequencies in the recorded data and to be able to construct a good  
2 starting model. Warner *et al.* (2013a) show anisotropic 3D FWI applied successfully to field  
3 data, and also demonstrate that the effects of elasticity and attenuation can be effectively  
4 minimized by appropriate amplitude normalization of both field and predicted seismic data.

5 Other challenges include determining the source, noise suppression, and the computational  
6 requirements of large models, large datasets and higher frequencies. The source can be  
7 determined directly from the data (Pratt *et al.* 1996; Warner *et al.* 2013a). Ambient noise is  
8 much less of a problem in data recorded at the ocean bottom than it is for towed-streamer  
9 data, and FWI appears to be extraordinarily robust against noise that is spatially incoherent  
10 due to the large redundancy in multi-azimuth data (e.g. Plessix 2008). Computational cost  
11 increases with model size, and as approximately the fourth power of the maximum  
12 frequency. The 3D Brazilian inversion took about three orders of magnitude more  
13 computational effort to run than would an equivalent 2D inversion over the same model.

14 A much-discussed issue when inverting field data is deciding which physics to use. In  
15 principle it is possible to use a full-elastic solution during inversion, and to invert for  
16 independent density and attenuation models. In practice, there is significant cross talk  
17 between the different parameters, and multi-parameter FWI is still an area of active research  
18 (Prioux *et al.* 2013). In the present context, we have previously conducted a suite of  
19 synthetic tests to explore the effects of modelling elastic data with an acoustic code, inverting  
20 using isotropic velocity models for anisotropic data, using a 2D approximation to invert 3D  
21 data, and not properly accounting for attenuation or density (Morgan *et al.* 2009; Warner *et al.*  
22 2012). Of these, the most significant effects were observed when using incorrect  
23 assumptions about anisotropy and when inverting complex 3D models using a 2D code –  
24 both of these can be properly overcome by using 3D anisotropic acoustic inversion. Inverting  
25 full-elastic data using an acoustic approximation produced results that were similar to those  
26 obtained when inverting acoustic data provided that both observed and predicted amplitudes  
27 were normalized appropriately during the inversion. Similar results were also obtained when  
28 inverting data generated with unknown attenuation and density models – provided that  
29 amplitude information is partially suppressed during the inversion, the resulting models are  
30 only minimally compromised by these unaccounted effects.

## 1 CONCLUSIONS

2 Three-dimensional acoustic anisotropic full-waveform inversion of airgun data, acquired  
3 using very long offsets, recorded on sparse ocean-bottom hydrophone arrays, is now able to  
4 recover high-resolution 3D velocity models of deep-crustal and whole-crustal targets of  
5 interest to the academic community, to the petroleum industry, and in geohazard  
6 assessment. The necessary field acquisition is feasible and affordable, and requires minimal  
7 modification to existing acquisition platforms. The necessary computer codes already exist;  
8 these have been developed for the petroleum industry, and have been proven against the  
9 ground truth of borehole data. We suggest that these developments, and the transfer of  
10 petroleum technology to address a wider range of problems, will be able to open up a new  
11 era of geophysical exploration of the Earth's crust. A necessary step is the acquisition of  
12 suitable medium-density, low-frequency, wide-azimuth, 3D field datasets of the type required  
13 for the application of this technology.

## 14 ACKNOWLEDGMENTS

15 Imperial College London wishes to thank the sponsors of the FULLWAVE consortia: BG, BP,  
16 Chevron, CGGVeritas, ConocoPhillips, DONG, ENI, HESS, Maersk, Nexen, Rio Tinto, TGS,  
17 Tullow Oil and Woodside for support in developing the 3D FWI software. We thank the PL  
18 534 partnership of BG Norge, Wintershall Norge, Statoil and Faroe Petroleum Norge for their  
19 kind permission to show the field data presented in Fig. 1, and the PL044 partnership:  
20 ConocoPhillips Skandinavia AS, Total E&P Norge AS, ENI Norge AS, Statoil Petroleum AS  
21 for their kind permission to use the data presented in Fig. 2. We gratefully acknowledge the  
22 contribution of CGG for processing the field data example presented in Fig. 1, and the  
23 assistance of Miles Evans, Andrew Ratcliffe, Graham Conroy, Richard Jupp and Andrew  
24 Irving of CGG. We gratefully acknowledge the help of James Selvage, BG Group, and Lucy  
25 Ramsey, BG Norge. The 3D ProMAX/SeisSpace package, supplied by Halliburton Software  
26 and Services, a Halliburton Company, under a university software grant, was used to  
27 preprocess and analyze the field and synthetic data. The inversion software used in this  
28 study is available for application to academic problems through collaboration with Imperial

- 1 College London, and to commercial partners through membership of the FULLWAVE
- 2 consortium.

## 1 REFERENCES

- 2 Bai, J. & Yingst, D., 2013. Q Estimation Through Waveform Inversion, *75<sup>th</sup> EAGE*  
3 *Conference*, Extended Abstracts.
- 4 Biondi, B. & Almomin, A., 2012. Tomographic full waveform inversion (TFWI) by combining  
5 full waveform inversion with wave-equation migration velocity analysis, *82<sup>nd</sup> Annual*  
6 *International meeting, SEG*, Expanded Abstracts.
- 7 Boudier, F., Nicolas, A. & Ildefonse, B., 1996. Magma chambers in the Oman ophiolite: fed  
8 from the top and the bottom, *Earth Planet. Sci. Lett.*, **144**, 239-250.
- 9 Brenders, A. J. & Pratt, R.G., 2007. Full waveform tomography for lithospheric imaging:  
10 results from a blind test in a realistic crustal model, *Geophys. J. Int.*, **168**, 133–151.
- 11 Bunks, C., Saleck, F.M., Zaleski, S. & Chavent, G., 1995. Multiscale seismic waveform  
12 inversion, *Geophysics*, **60**, 1457-1473.
- 13 Contrucci, I., Matias, L., Moulin, M., Géli, L., Klingelhofer, F., Nouzé, H., Aslanian, D., Olivet,  
14 J., Réhault, J. & Sibuet, J., 2004. Deep structure of the West African continental margin  
15 (Congo, Zaïre, Angola), between 5°S and 8°S, from reflection/refraction seismics and gravity  
16 data, *Geophys. J. Int.*, **158**, 529-553.
- 17 Christeson, G. L., Nakamura, Y., Buffler, R., Morgan, J. & Warner, M., 2001. Deep crustal  
18 structure of the Chicxulub impact crater, *J. Geophys. Res.*, **106**, 21751–21769.
- 19 Christeson, G. L., Mann, P., Escalona, A. & Aitken, T.J., 2008. Crustal structure of the  
20 Caribbean-northeastern South America arc-continent collision zone, *J. Geophys. Res.*, **113**,  
21 B08104. doi:10.1029/2007JB005373.
- 22 Detrick, R.S., Buhl, P., Vera, E., Mutter, J., Orcutt, J., Madsen, J. & Brocher, T., 1987.  
23 Multichannel seismic imaging of a crustal magma chamber along the East Pacific Rise  
24 between 9°N and 13°N, *Nature*, **326**, 35-41.

- 1 Dunn, R.A., Toomey, D.R. & Solomon, S.C., 2000. Seismic structure and physical properties  
2 of the crust and shallow mantle beneath the East Pacific Rise, *J. Geophys. Res.*, **94**, 23537–  
3 23555.
- 4 Elsworth, D., Mattioli, G., Taron, J., Voight, B. & Herd, R., 2008. Implications of Magma  
5 Transfer Between Multiple Reservoirs on Eruption Cycling, *Science*, **322**, 246.
- 6 Fraga, C.T. da Costa, Borges, F.A., Bellot, C., Beltrão, R. & Assayag, M.I., 2003. Campos  
7 Basin – 25 Years of Production and its Contribution to the Oil Industry, *Offshore Technology*  
8 *Conference*, Houston Texas, 15219.
- 9 Foroozan, R., Elsworth, D., Voight, B. & Mattioli, G.S., 2010. Dual reservoir structure at  
10 Soufrière Hills Volcano inferred from continuous GPS observations and heterogeneous  
11 elastic modeling, *Geophys. Res. Lett.*, **37**, L00E12, doi:10.1029/2010GL042,511.
- 12 Granli, J. R., Arntsen, B., Sollid, A. & Hilde, E. 1999., Imaging through gas-filled sediments  
13 using marine shear-wave data, *Geophysics*, **64**, 668–677.
- 14 Greenhalgh, J., Wells, S., Borsato, R., Pratt, D., Martin, M., Roberson, R., Fontes, C. &  
15 Obaje, W. A., 2011. A fresh look at prospectivity of the Equatorial Conjugate Margin of Brazil  
16 and Africa, *First Break*, **29** (11), 67-72.
- 17 Guasch, L., Warner, M., Nangoo, T., Morgan, J., Umpleby, A., Stekl, I. & Shah, N., 2012.  
18 Elastic 3D full-waveform inversion, *82<sup>nd</sup> Annual International meeting, SEG*, Expanded  
19 Abstracts.
- 20 Henstock, T.J., Woods, A. & White, R.S., 1993. The accretion of oceanic crust by episodic  
21 sill intrusion, *J. Geophys. Res.*, **98**, 4143-4161.
- 22 Houbiers, M., Mispel, J., Knudsen, B.E. & Amundsen, L., 2013. FWI with OBC Data From  
23 the Mariner Field, UK – The Impact on Mapping Sands at Reservoir Level, *75<sup>th</sup> EAGE*  
24 *Conference*, Extended Abstracts. DOI: 10.3997/2214-4609.20130829
- 25 Jones, C.E., Evans, M., Ratcliffe, A., Conroy, G., Jupp, R., Selvage, J.I. & Ramsey, L., 2013.  
26 Full Waveform Inversion in a Complex Geological Setting - A Narrow Azimuth Towed

- 1 Streamer Case Study from the Barents Sea, 75<sup>th</sup> EAGE Conference, Extended Abstracts.  
2 DOI: 10.3997/2214-4609.20130830
- 3 Kapoor, S., Vigh, D., Li, H. & Derharoutian, D., 2012. Full Waveform Inversion for Details  
4 Velocity Model Building, 74<sup>th</sup> EAGE Conference, Extended Abstracts.
- 5 Kapoor, S., Vigh, D., Wiarda, E. & Alwon, S., 2013. Full Waveform Inversion Around the  
6 World, 75<sup>th</sup> EAGE Conference, Extended Abstracts. DOI: 10.3997/2214-4609.20130827.
- 7 Korenaga, J. & Kelemen, P.B., 1998. Melt migration through the oceanic lower crust: A  
8 constraint from melt percolation modeling with finite solid diffusion, *Earth Planet. Sci. Lett.*,  
9 **156**, 1-11.
- 10 Lu, R., Lazaratos, S., Wang, K., Cha, Y.H., Chikichev, I. & Prosser, R., 2013. High-  
11 resolution Elastic FWI for Reservoir Characterization, 75<sup>th</sup> EAGE Conference, Extended  
12 Abstracts. DOI: 10.3997/2214-4609.20130113
- 13 Lua, K.W.H., White, R.S. & Christie, P.A.F., 2007. Low-frequency source for long-offset,  
14 sub-basalt and deep crustal penetration, *The Leading Edge*, **28**, 36-39.
- 15 Lavier, L. & Manatschal, G., 2006. A mechanism to thin the continental lithosphere at  
16 magma-poor margins, *Nature*, **440**, 7082, 324-328. 10.1016/j.jvolgeores.2007.06.008.
- 17 Lazaratos, S., Chikichev, I. & Wang, K., 2011. Improving the Convergence Rate of Full  
18 Wavefield Inversion Using Spectral Shaping, 81<sup>st</sup> Annual International meeting, SEG,  
19 Expanded Abstracts.
- 20 MacLennan, J., Hulme, T. & Singh, S.C., 2004. Thermal models of oceanic crustal accretion:  
21 Linking geophysical, geological and petrological observations, *Geochem. Geophys.*  
22 *Geosyst.*, **5**, doi: 10.1029/2003GC000605.
- 23 MacLeod, C. & Yaouancq, G., 2000. A fossil melt lens in the Oman ophiolite: implications for  
24 magma chamber processes at fast spreading ridges, *Earth Planet. Sci. Lett.*, **176**, 357-373.
- 25 Mattioli, G. S., Herd, R.A., Strutt, M.H., Ryan, G., Widiwijayanti, C. & Voight, B., 2010. Long



term surface deformation of Soufrière Hills Volcano, Montserrat from GPS geodesy:  
Inferences from simple elastic inverse models, *Geophys. Res. Lett.*, **442**, 37 (L00E13),  
doi:10.1029/2009GL042268

Mohriak, W. U., Hobbs, R. & Dewey, J.F., 1990. Basin-forming processes and the deep  
structure of the Campos Basin, offshore Brazil, *Marine Petroleum Geol.*, **7**, 94-122.

Morgan, J., Warner, M. & the Chicxulub Working Group, 1997. Size and morphology of the  
Chicxulub impact crater, *Nature*, **390**, 472–476.

Morgan, J.V., Christeson, G.L. & Warner M., 2009. Using swath bathymetry as an a priori  
constraint in a 3D full wavefield tomographic inversion of seismic data across oceanic crust,  
*Eos. Trans. AGU*, **90**(52), Fall Meet. Suppl., Abstract S11C-07.

Morgan, J.V., Warner, M.R., Collins, G.S., Grieve, R.A.F., Christeson, G.L., Gulick, S.P.S. &  
Barton, P.J., 2011. Full waveform tomographic images of the peak ring at the Chicxulub  
impact crater, *J. Geophys. Res.*, **116**, DOI: 10.1029/2010JB008015

Mothi, S., Schwarz, K. & Zhu, H., 2013. Impact of full-azimuth and long-offset acquisition on  
full waveform inversion in deep water Gulf of Mexico, *75<sup>th</sup> EAGE Conference*, Extended  
Abstracts. DOI: 10.3997/2214-4609.20130826

Mutter, J. C., Carbotte, S., Su, W., Xu, L., Buhl, P., Detrick, R.S, Kent, G., Orcutt, J. &  
Harding, A., 1995. Seismic images of active magma systems beneath the East Pacific Rise  
17°00 to 17°35'S, *Science*, **268**, 391-395, 1995.

Paulatto, M., Annen, C., Henstock, T.J., Kiddle., E., Minshull, T.A., Sparks, R.S.J. & Voight,  
B., 2012. Magma chamber properties from integrated seismic tomography and thermal  
modeling at Montserrat, *Geochem. Geophys. Geosyst.*, **13**, Q01014.  
doi:10.1029/2011GC003892.

Phipps Morgan, J. & Chen, Y.J., 1993. The genesis of oceanic crust: Magma injection,  
hydrothermal circulation, and crustal flow, *J. Geophys. Res.*, **98**, 6283-6297.

Plessix, R.-E., 2008. Introduction: Towards a full waveform inversion, *Geophys. Prospect.*,

1    **56**, 761-763.

2    Plessix, R.-E. & Perkins, C., 2010. Full waveform inversion of a deep water ocean bottom  
3    seismometer dataset, *First Break*, **28** (4), 71-78.

4    Pratt, R. G., Song, Z.-M., Williamson, P. & Warner, M., 1996. Two-dimensional velocity  
5    models from wide-angle seismic data by wavefield inversion, *Geophys. J. Int.*, **124**, 323–340,  
6    doi: 10.1111/gji.1996.124.

7    Pratt, R. G., 1999. Seismic waveform inversion in the frequency domain, Part I: Theory and  
8    verification in a physical scale model, *Geophysics*, **64**, 888–901.

9    Pratt, R. G. & Shipp, R. M., 1999. Seismic waveform inversion in the frequency domain, Part  
10    2: Fault delineation in sediments using crosshole data, *Geophysics*, **64**, 901–913, doi:  
11    10.1190/1.1444598.

12    Prieux, V., Brossier, R., Gholami, Y., Operto, S., Virieux, J., Barkved, O.I. & Kommedal, J.H.,  
13    2011. On the footprint of anisotropy on isotropic full waveform inversion: the Valhall case  
14    study, *Geophys. J. Int.*, **187**, 1495–151.

15    Prieux, V., Brossier, R., Operto, S. & Virieux, J., 2013. Multi-parameter full waveform  
16    inversion of multi-component ocean bottom cable data from the Valhall field. Part 1. Imaging  
17    compressional wave speed density and attenuation, *Geophys. J. Int.*, doi: 10.1093/gji/ggt177.

18    Ratcliffe, A., Win, C., Vinje, V., Conroy, G., Warner, M., Umpleby, A., Štekl, I., Nangoo, T. &  
19    Bertrand, A., 2011. Full waveform inversion: A North Sea OBS case study, *81<sup>st</sup> Annual*  
20    *International meeting, SEG*, Expanded Abstracts, 2384–2388.

21    Sambridge, M. & Mosegaard, K., 2002. Monte Carlo methods in geophysical inverse  
22    problems, *Rev. Geophys.*, **40**, 1–29.

23    Selwood, C.S., Shah, H.M., Mika, J.E. & Baptiste, D., 2013. The Evolution of Imaging over  
24    Azeri, from TTI Tomography to Anisotropic FWI, *75<sup>th</sup> EAGE Conference*, Extended  
25    Abstracts. DOI: 10.3997/2214-4609.20130831.

- 1 Shah, N.K., Washbourne, J.K & Bube, K.P., 2012a. System and Method for Data Inversion  
2 with Phase Unwrapping, *International patent application*, PCT/US2012/028470.
- 3 Shah, N., Warner, M., Nangoo, T., Umpleby, A., Štekl, I., Morgan, J. & Guasch, L., 2012b.  
4 Quality assured full-waveform inversion: Ensuring starting model adequacy, *82<sup>nd</sup> Annual*  
5 *International Meeting, SEG*, Expanded Abstracts.
- 6 Shah, N., 2013. Robust Full Waveform Inversion. *PhD Thesis*, Imperial College London, UK.
- 7 Shipp, R.M. & Singh, S.C., 2002. Two-dimensional full wavefield inversion of wide-aperture  
8 marine seismic streamer data, *Geophys. J. Int.*, **151**, 325–344.
- 9 Singh, S. C., Harding, A., Kent, G., Sinha, M. C., Combier, V., Hobbs, R., Barton, P., White,  
10 R., Tong, V., Pye, J. & Orcutt, J. A., 2006. Seismic reflection images of Moho underlying  
11 melt sills at the East Pacific Rise, *Nature*, **442**, 287-290.
- 12 Sirgue, L. & Pratt, R.G., 2004. Efficient waveform inversion and imaging: a strategy for  
13 selecting temporal frequencies, *Geophysics*, **69**, 231–248
- 14 Sirgue, L., 2006. The importance of low frequency and large offset in waveform inversion,  
15 *68<sup>th</sup> Annual International Conference and Exhibition, EAGE*, Extended Abstracts, A037.
- 16 Sirgue, L., Etgen, J. & Albertin, U., 2007. 3D full waveform inversion: Wide versus narrow  
17 azimuth acquisitions, *77<sup>th</sup> Annual International Meeting, SEG*, Expanded Abstracts, 1760–  
18 1764.
- 19 Sirgue, L., Barkved, O.I., Dellinger, J., Etgen, J., Albertin, U. & Kommedal, J.H., 2010. Full  
20 waveform inversion: the next leap forward in imaging at Valhall, *First Break*, **28** (4), 65-70.
- 21 Solano, J., Jackson, M.D., Sparks, R.S.J., Blundy, J.D. & Annen, C., 2012. Melt segregation  
22 in Deep Crustal Hot Zones: A mechanism for chemical differentiation, crustal assimilation  
23 and the formation of evolved magmas, *J. Petrology*, **53**, 1999-2026.
- 24 Tarantola, A., 1984. Inversion of seismic reflection data in the acoustic approximation:  
25 *Geophysics*, **49**, 1259-1266.

- 1 Unternehr, P., Peron-Pinvidic, G., Manatschal, G. & Sutra, E., 2010. Hyper-extended crust in  
2 the South Atlantic: in search of a model, *Petroleum Geosci.*, **16**, 207-215.
- 3 Urick, R.J., 1984. Ambient Noise in the Sea. *Published by Undersea Warfare Technology*  
4 *Office, Naval Sea System Command, Department of the Navy, Washington DC.*
- 5 van Leeuwen, T. & Herrmann, F.J., 2013. Mitigating local minima in full-waveform inversion  
6 by expanding the search space, *Geophys. J. Int.*, Published on-line July 30, 2013. DOI:  
7 10.1093/gji/ggt258.
- 8 Vigh, D., Starr, B., Kapoor, J. & Li, H., 2010. 3D Full waveform inversion of Gulf of Mexico  
9 WAZ dataset, *80<sup>th</sup> Annual International Meeting, SEG*, Expanded Abstracts, 957-961.
- 10 Vigh, D., Kapoor, J. & Li, H., 2011. Full waveform inversion application in different geological  
11 settings, *81<sup>st</sup> Annual International Meeting, SEG*, Expanded Abstracts, 2374-2378.
- 12 Vigh, D., Jiao, K., Huang, M., Moldoveanu, N. & Kapoor, J., 2013a. Long-offset-aided Full-  
13 waveform Inversion, *75<sup>th</sup> EAGE Conference*, Extended Abstracts. DOI: 10.3997/2214-  
14 4609.20130825
- 15 Vigh, D., Jiao, K. & Watts, D., 2013b. Elastic Full-waveform Inversion Using 4C Data  
16 Acquisition, *75<sup>th</sup> EAGE Conference*, Extended Abstracts. DOI: 10.3997/2214-  
17 4609.20130114
- 18 Virieux, J. & Operto, S., 2009. An overview of full-waveform inversion in exploration  
19 geophysics, *Geophysics*, **74**, WCC1-WCC26.
- 20 Voight, B., Widiwijayanti, C., Mattioli, G., Elsworth, D., Hidayat, D. & Strutt, M.H., 2010.  
21 Magma-sponge hypothesis and stratovolcanoes: Case for a compressible reservoir and  
22 quasi-steady deep influx at Soufrière Hills Volcano, Montserrat, *Geophys. Res. Lett.*, **37**,  
23 L00E05. doi:10.1029/2009GL041732.
- 24 Warner, M.R., Morgan, J.V., Umpleby, A., Štekl, I. & L. Guasch, L., 2012. Which physics for  
25 full-wavefield inversion?, *74<sup>th</sup> Annual International Conference and Exhibition, EAGE*,  
26 Extended Abstracts, W029.

- 1 Warner, M.R., Ratcliffe, A., Nangoo, T., Morgan, J., Umpleby, A., Shah, N., Vinje, V., Štekl,  
2 I., Guasch, L., Win, C., Conroy, G. & Bertrand, A., 2013a. Anisotropic 3D full-waveform  
3 inversion, *Geophysics*, **78**, 10.1190/GEO2012-0338.1
- 4 Warner, M., Nangoo, T., Shah, N., Umpleby, A. & Morgan, J., 2013b. Full-waveform  
5 inversion of cycle-skipped seismic data by frequency down-shifting, *83<sup>rd</sup> Annual International*  
6 *Meeting, SEG*, Expanded Abstracts.
- 7 White, N., Thompson, M. & Barwise, T., 2003. Understanding the thermal evolution of deep-  
8 water continental margins, *Nature*, **426**, 334-343.
- 9 Williamson, P. R., 1991. A guide to the limits of resolution imposed by scattering in ray  
10 tomography, *Geophysics*, **56**, 202–207, doi: 10.1190/1.1443032.
- 11 Woodward, M. J., Nichols, D., Zdraveva, O., Whitfield, P. & Johns, T., 2008. A decade of  
12 tomography, *Geophysics*, **73**, VE5–VE11.
- 13 Xu, S., Wang, D., Chen, F., Zhang, F. & Lambare, G., 2012. Full Waveform Inversion for  
14 Reflected Seismic Data, *74<sup>th</sup> EAGE Conference*, Extended Abstracts.
- 15 Zellmer, G. F., Sparks, R.S.J., Hawkesworth, C.J. & Wiedenbeck, M., 2003. Magma  
16 Emplacement and Remobilization Timescales Beneath Montserrat: Insights from Sr and Ba  
17 Zonation in Plagioclase, *J. Petrology*, **44**, 1413–1431.
- 18 Zelt, C. A., 2011. Traveltime tomography using controlled-source seismic data, in  
19 *Encyclopedia of Solid Earth Geophysics, Volume 2*, Springer, H.K. Gupta (editor), p1453-  
20 1473.
- 21 Ziolkowski, A.M., 1986. The scaling of airgun arrays, including depth dependence and  
22 interactions, *Geophys. Prospect.*, **34**, 383–408.

## Figure 1

Horizontal slices through the Samson Dome. Left-hand slices are at a depth below surface of 1100 m; those on the right are at 1350 m.

(a) The starting velocity model.

(b) The recovered FWI velocity model.

(c) The FWI model overlain by the reflection image migrated with the starting model.

## Figure 2

Field data acquired using conventional airguns and recorded on ocean-bottom hydrophones. Left-hand panels show a shot record, in the time domain, for a single ocean-bottom cable, after application of a 8 Hz low-cut filter; (a) and (b) show the same gather without and with a time window. The centre and right-hand panels show phase plots for a single receiver gather, viewed in the frequency domain at a single frequency of 2 or 3 Hz. The receiver is at the centre of the circular features, and colours represent the phase of a particular shot. Data in the top two panels have not been windowed; data in the bottom two panels have been windowed around the early refracted arrivals. Spatially coherent structure on receiver gathers is indicative of source-generated signal. There is good signal-to-noise in the windowed transmitted arrivals at 2 Hz. Analysis and data from Shah (2013) and Warner *et al.* (2013).

## Figure 3

Vertical slice through the 3D travel-time tomographic velocity model of Paulatto *et al.* (2012); velocities are in  $\text{km s}^{-1}$  and contours are  $100 \text{ m s}^{-1}$  apart. The low-velocity region beneath the Soufrière Hills Volcano (SHV) at 5-8 km depth is interpreted to represent a crustal magma chamber.

#### **Figure 4**

P-wave velocity models over the Soufrière Hills Volcano. Top and sides show internal slices through the magma chambers as indicated by dashed lines.

a) Model used to generate synthetic data for subsequent FWI.

b) Model recovered after 3D FWI. The starting model did not contain the magma chambers. FWI recovers the upper chamber accurately, and recovers the location and relative velocity perturbation within the lower chamber.

#### **Figure 5**

Velocity profiles through the centre of the magma chamber.

Solid line shows the difference between the true and starting velocity models; dashed and dotted lines show the difference between the FWI recovered and starting models after the 3<sup>rd</sup>, 18<sup>th</sup> and 36<sup>th</sup> iteration.

#### **Figure 6**

Checkerboard tests beneath Montserrat

a) Vertical slice through the 3D Montserrat model with checkerboard added.

b) and c) Vertical slices through the original and recovered checkerboard.

d) and e) Horizontal slices through the original and recovered checkerboard.

## **Figure 7**

A geological interpretation of a time-migrated seismic reflection profile across the continental slope of the Campos Basin (redrawn from Unternehr *et al.*, 2010). The uppermost sediments and top salt are well-resolved, but there is minimal reflectivity in the sag-basin sediments and the locations of the basement, continental-oceanic boundary and crustal thickness are unclear in the reflection data.

## **Figure 8**

a) The velocity model used to generate synthetic data for FWI. Structures have been added in the sag-basin sediments to represent hydrocarbon exploration targets. The continental-oceanic boundary is represented by a sharp transition, and layering has been added to the anomalous mantle to represent sill intrusions.

b) The starting velocity model for FWI.

c) Recovered velocity model after FWI using 441 receivers.

d) Recovered model using only 90 receivers.

Inset shows a 1D velocity profile close to the centre of the model and marked by the arrow.

Right-hand trace is the true minus the starting model, and the left hand trace is the recovered minus the starting model.

## **Figure 9**

a) A vertical slice through the 3D Brazil model with checkerboard added.

b) and c) Vertical slices through the original and recovered checkerboard.

d) and e) Horizontal slices through the original and recovered checkerboard.



**Figure 10**

End member models for the accretion of lower oceanic crust:

(a) Gabbro glacier (Henstock *et al.* 1993; Phipps Morgan and Chen 1993).

(b) Sheeted sills (Korenaga and Kelemen 1998; MacLeod and Yaouancq 2000).

**Figure 11**

Vertical slice through 3D velocity model of the East Pacific Rise.

a) Long-wavelength background model.

b) With added checkerboards in upper crust, lower crust and uppermost mantle.

**Figure 12**

a) Horizontal slice through the checkerboard perturbation in the uppermost mantle immediately below the Moho beneath the East Pacific Rise.

b) Receiver locations on the seabed above the East Pacific Rise. The majority of the synthetic experiments used the array shown in yellow. The results shown in Fig. 14d used the reduced-area array shown in green.

**Figure 13**

Synthetic seismograms generated using the model shown in Fig. 11.

a) Acoustic modelling. Trace amplitudes are weighted linearly with increasing offset but are otherwise shown at true amplitude.

b) Acoustic modelling after low-pass filtering and time windowing to match the bandwidth and data used for FWI. This record shows the full offset range of the data. The data have been amplitude normalised, trace by trace, after filtering and windowing – these are the data to which transmission FWI is typically applied.

c) Elastic modelling corresponding to (a).

1 d) Elastic modelling corresponding to (b).

2

### 3 **Figure 14**

4 Recovered checkerboards in the mantle corresponding to Fig. 12.

5 a) Inverting all the data.

6 b) Inverting time-windowed data.

7 c) Inverting time-windowed data with added noise.

8 d) Inverting data from receivers that are clustered towards the left side of the model, green  
9 receivers in Fig. 12b.

10

### 11 **Figure 15**

12 Recovered checkerboards obtained using starting models that have systematic errors.

13 a) The starting model was everywhere fast, and the predicted travel times at 10 s were 200  
14 ms early. The inversion started at 1 Hz.

15 b) The starting model was everywhere fast, and the predicted travel times at 10 s were 400  
16 ms early. The inversion started at 1 Hz

17 c) Starting model as (a). The inversion started at 2.4 Hz.

18 d) Starting model as (b). The inversion started at 2.4 Hz.

19

### 20 **Figure 16**

21 Recovered checkerboard obtained from elastic synthetic data.

22 a) Using acoustic inversion.

23 b) Using elastic inversion assuming a fixed relationship between P-wave and S-wave  
24 velocity.

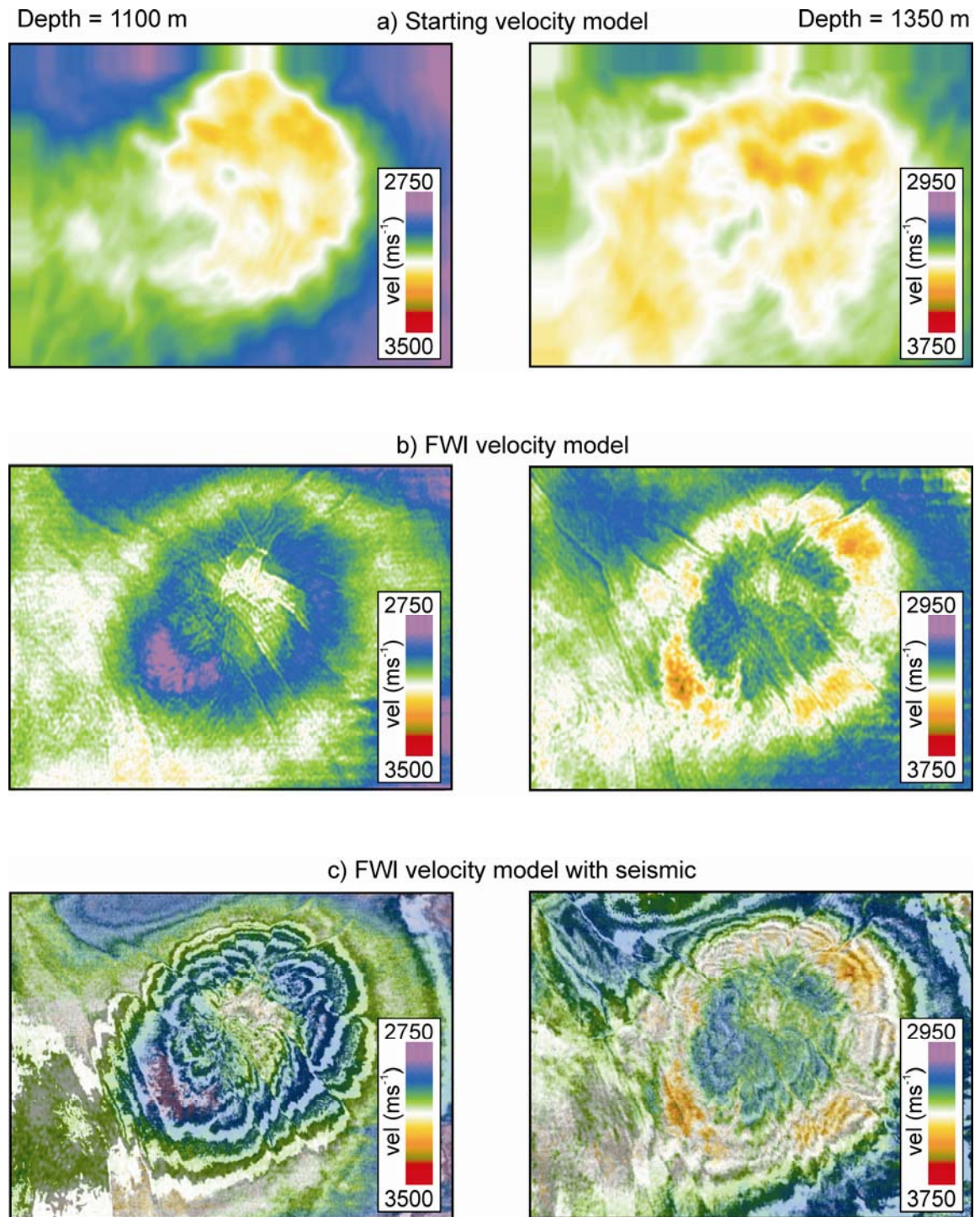


**Figure 1** Horizontal slices through the Samson Dome. Left-hand slices are at a depth below surface of 1100 m; those on the right are at 1350 m.

(a) The starting velocity model.

(b) The recovered FWI velocity model.

(c) The FWI model overlain by the reflection image migrated with the starting model.

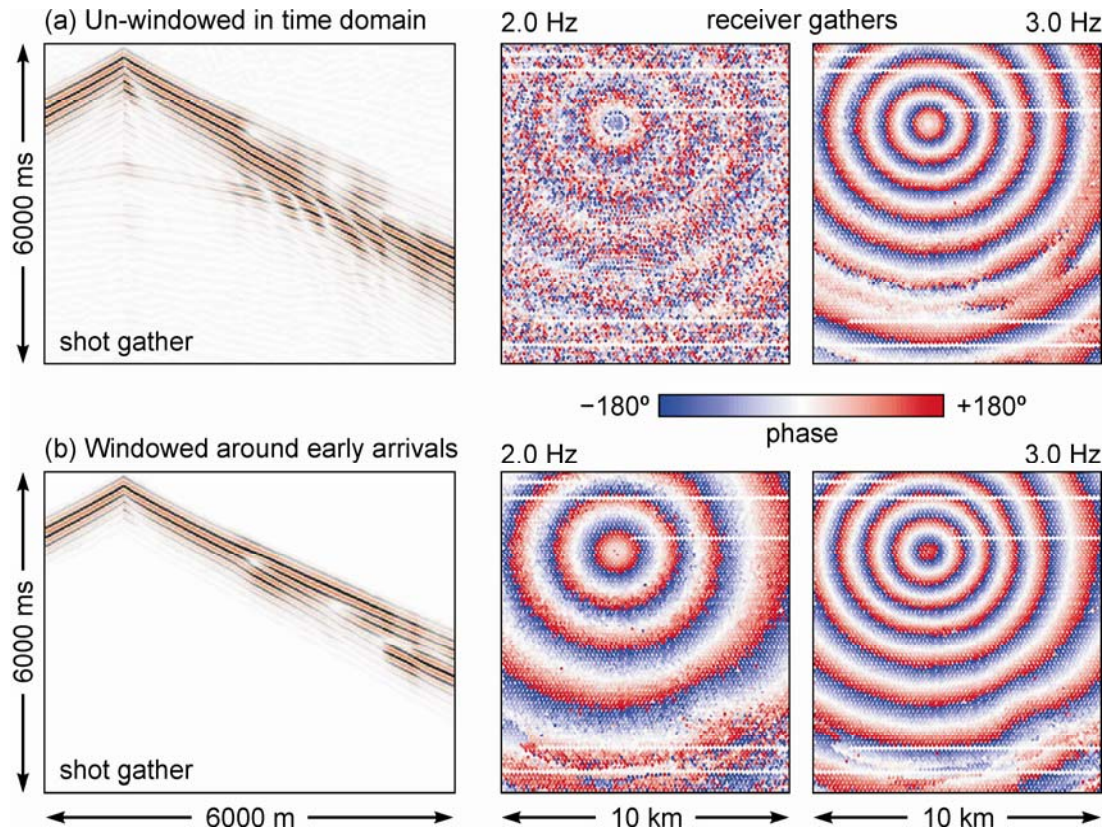


**Figure 2**

Field data acquired using conventional airguns and recorded on ocean-bottom hydrophones. Left-hand panels show a shot record, in the time domain, for a single ocean-bottom cable, after application of a 8 Hz low-cut filter; (a) and (b) show the same gather without and with a time window. The centre and right-hand panels show phase plots for a single receiver gather, viewed in the frequency domain at a single frequency of 2 or 3 Hz. The receiver is at the centre of the circular features, and colours represent the phase of a particular shot. Data in the top two panels have not been windowed; data in the bottom two panels have been windowed around the early refracted arrivals. Spatially coherent structure on receiver gathers is indicative of source-generated signal. There is good signal-to-noise in the windowed transmitted arrivals at 2 Hz. Analysis and data from Shah (2013) and Warner *et al.* (2013).

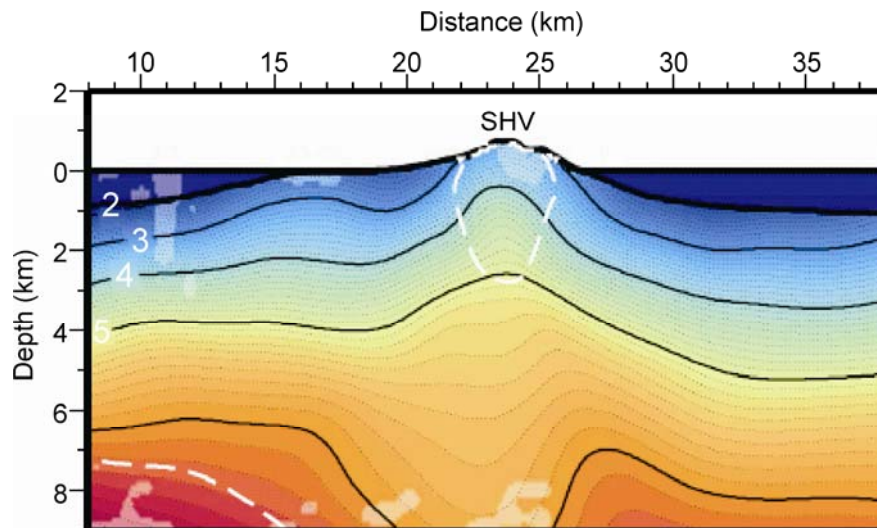


**Figure 3**

Vertical slice through the 3D travel-time tomographic velocity model of Paulatto *et al.* (2012); velocities are in  $\text{km s}^{-1}$  and contours are  $100 \text{ m s}^{-1}$  apart. The low-velocity region beneath the Soufrière Hills Volcano (SHV) at 5–8 km depth is interpreted to represent a crustal magma chamber.



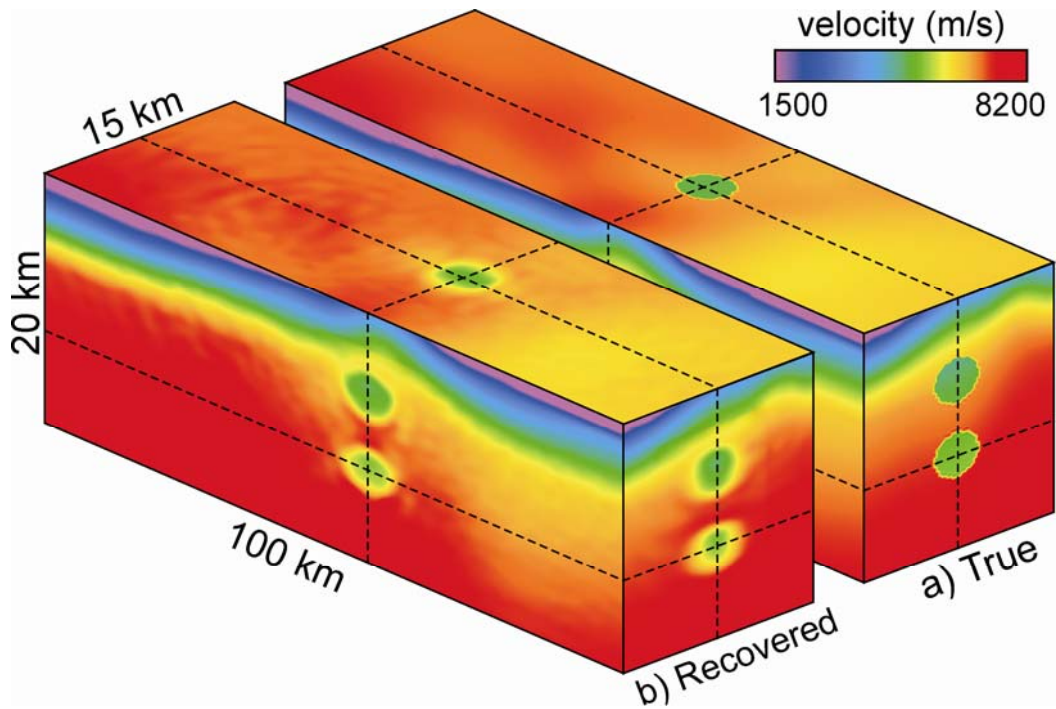


**Figure 4**

P-wave velocity models over the Soufrière Hills Volcano. Top and sides show internal slices through the magma chambers as indicated by dashed lines.

a) Model used to generate synthetic data for subsequent FWI.

b) Model recovered after 3D FWI. The starting model did not contain the magma chambers. FWI recovers the upper chamber accurately, and recovers the location and relative velocity perturbation within the lower chamber.

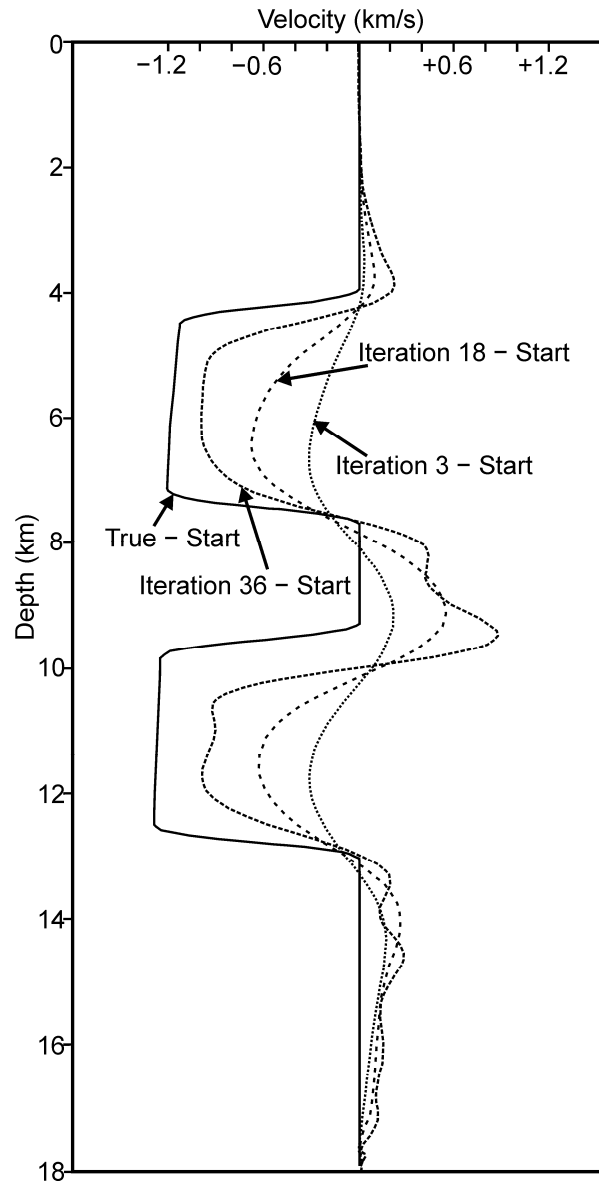


**Figure 5**

Velocity profiles through the centre of the magma chamber.

Solid line shows the difference between the true and starting velocity models; dashed and dotted lines show the difference between the FWI recovered and starting models after the 3<sup>rd</sup>, 18<sup>th</sup> and 36<sup>th</sup> iteration.

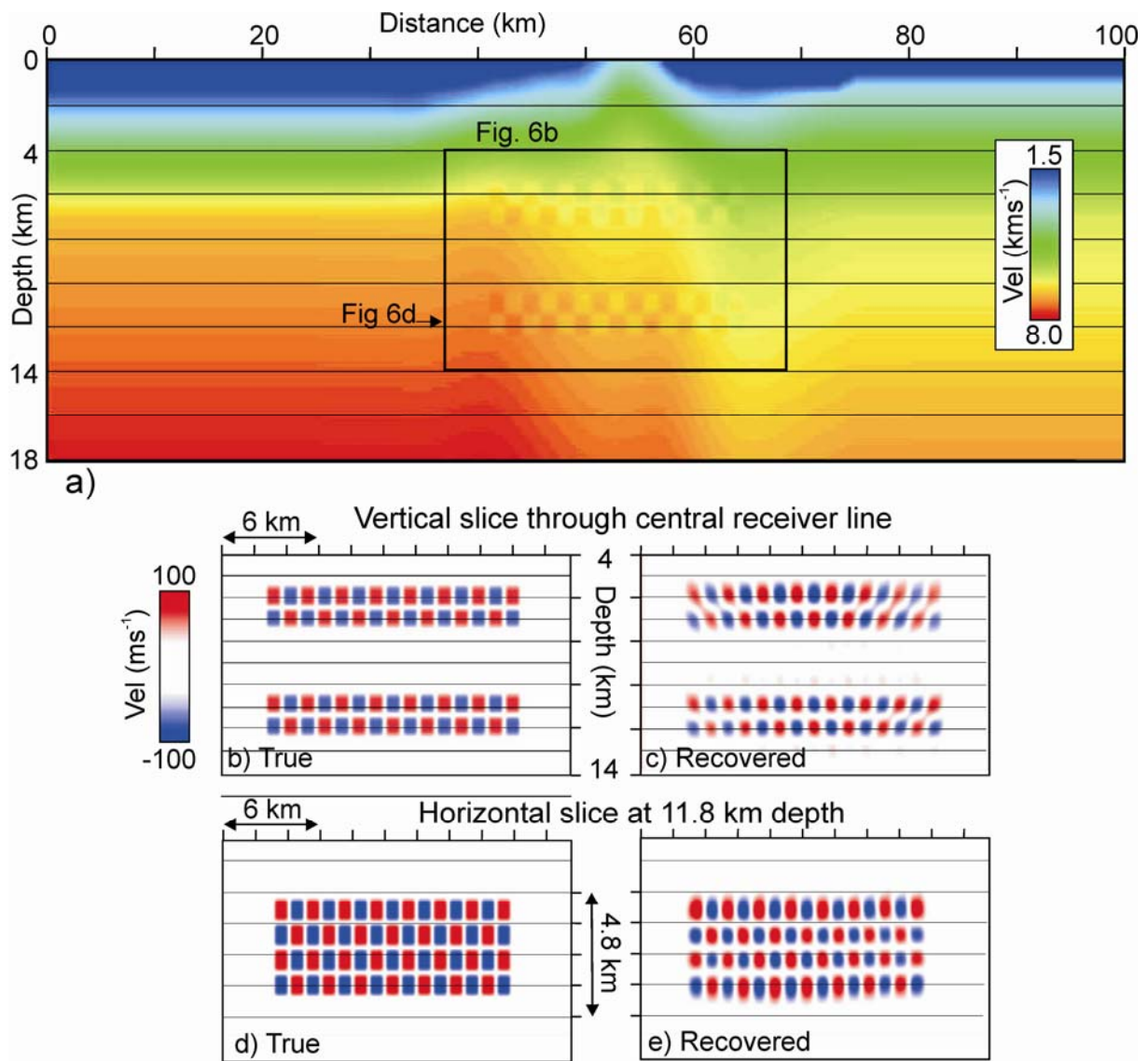


**Figure 6**

Checkerboard tests beneath Montserrat

a) Vertical slice through the 3D Montserrat model with checkerboard added.

b) and c) Vertical slices through the original and recovered checkerboard.

d) and e) Horizontal slices through the original and recovered checkerboard.



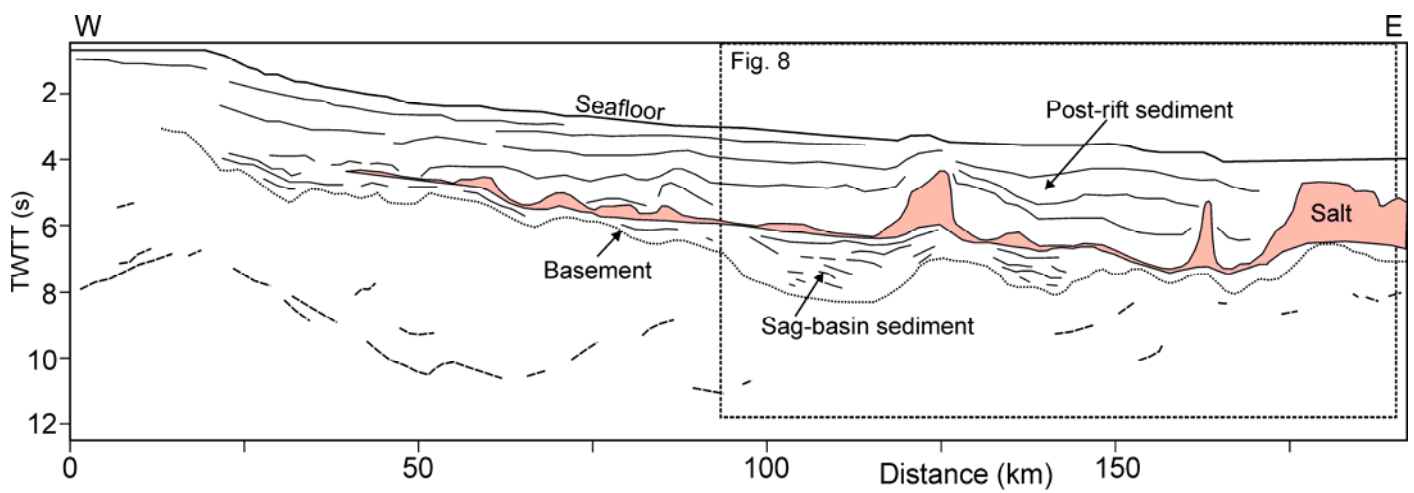


**Figure 7**

A geological interpretation of a time-migrated seismic reflection profile across the continental slope of the Campos Basin (redrawn from Unternehr *et al.*, 2010). The uppermost sediments and top salt are well-resolved, but there is minimal reflectivity in the sag-basin sediments and the locations of the basement, continental-oceanic boundary and crustal thickness are unclear in the reflection data.

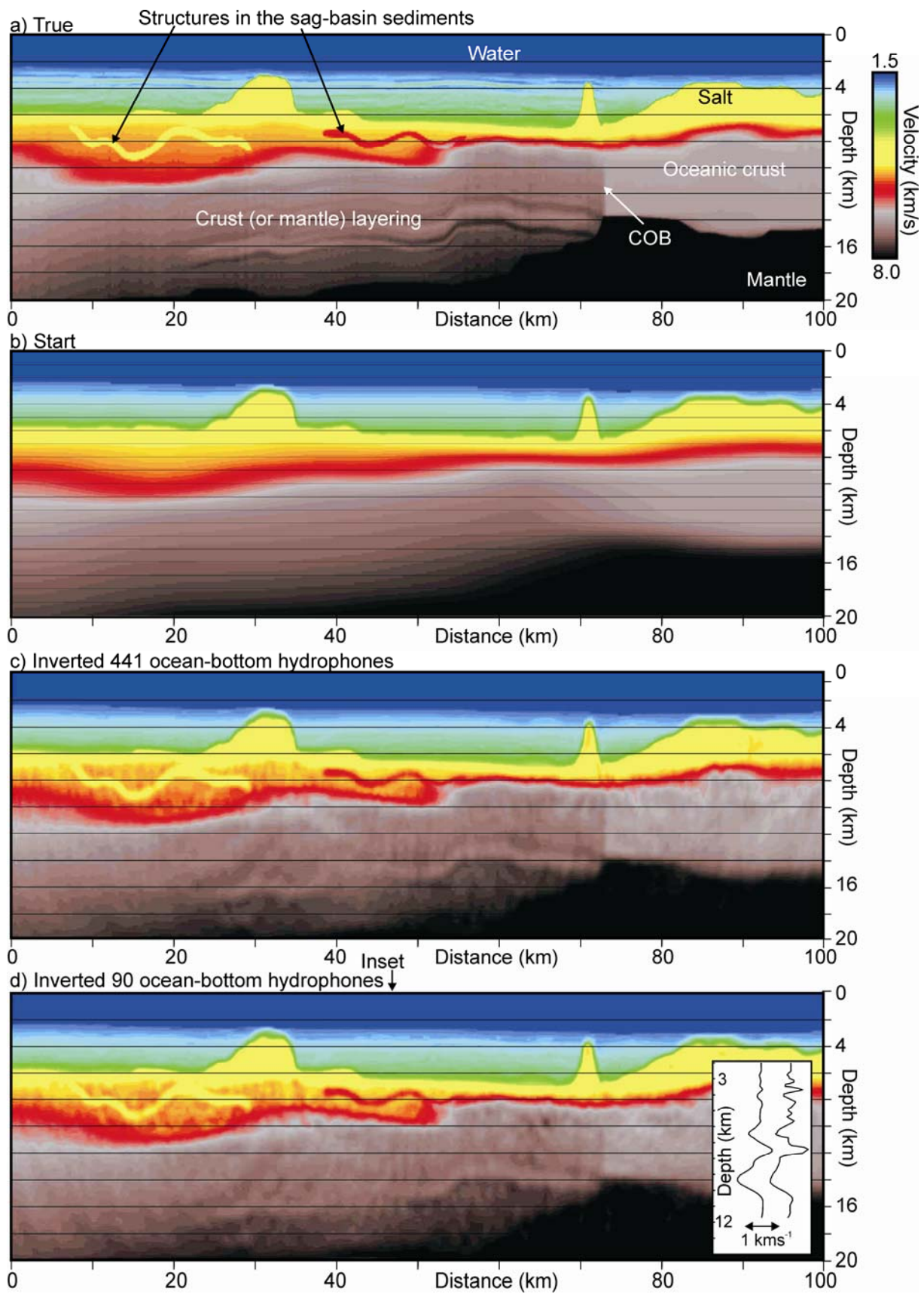


## Figure 8

a) The velocity model used to generate synthetic data for FWI. Structures have been added in the sag-basin sediments to represent hydrocarbon exploration targets. The continental-oceanic boundary is represented by a sharp transition, and layering has been added to the anomalous mantle to represent sill intrusions.

b) The starting velocity model for FWI.

c) Recovered velocity model after FWI using 441 receivers.

d) Recovered model using only 90 receivers.

Inset shows a 1D velocity profile close to the centre of the model and marked by the arrow. Right-hand trace is the true minus the starting model, and the left hand trace is the recovered minus the starting model.

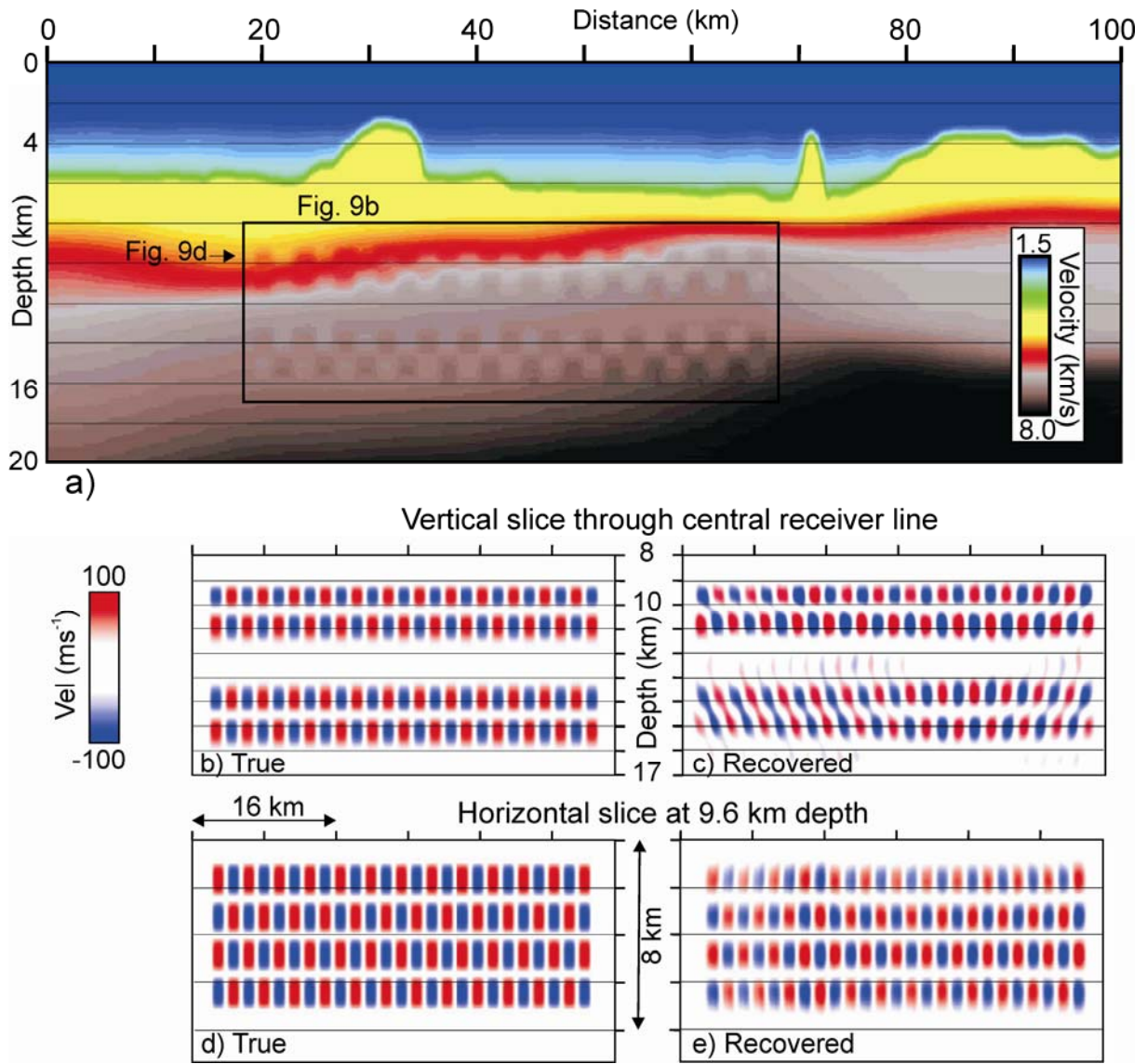


**Figure 9**

a) A vertical slice through the 3D Brazil model with checkerboard added.

b) and c) Vertical slices through the original and recovered checkerboard.

d) and e) Horizontal slices through the original and recovered checkerboard.

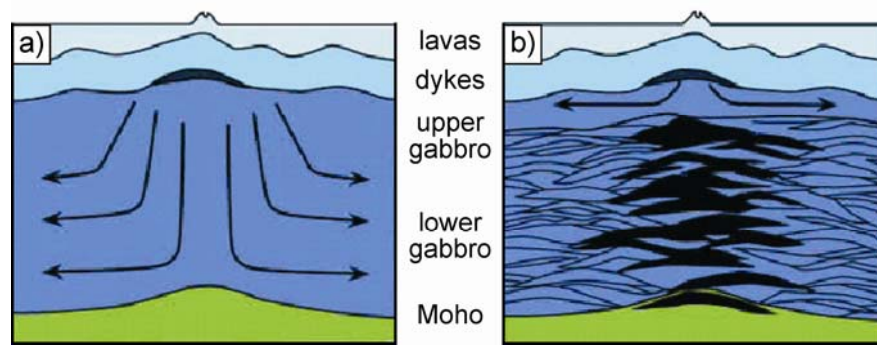


**Figure 10**

End member models for the accretion of lower oceanic crust:

(a) Gabbro glacier (Henstock *et al.* 1993; Phipps Morgan and Chen 1993).

(b) Sheeted sills (Korenaga and Kelemen 1998; MacLeod and Yaouancq 2000).

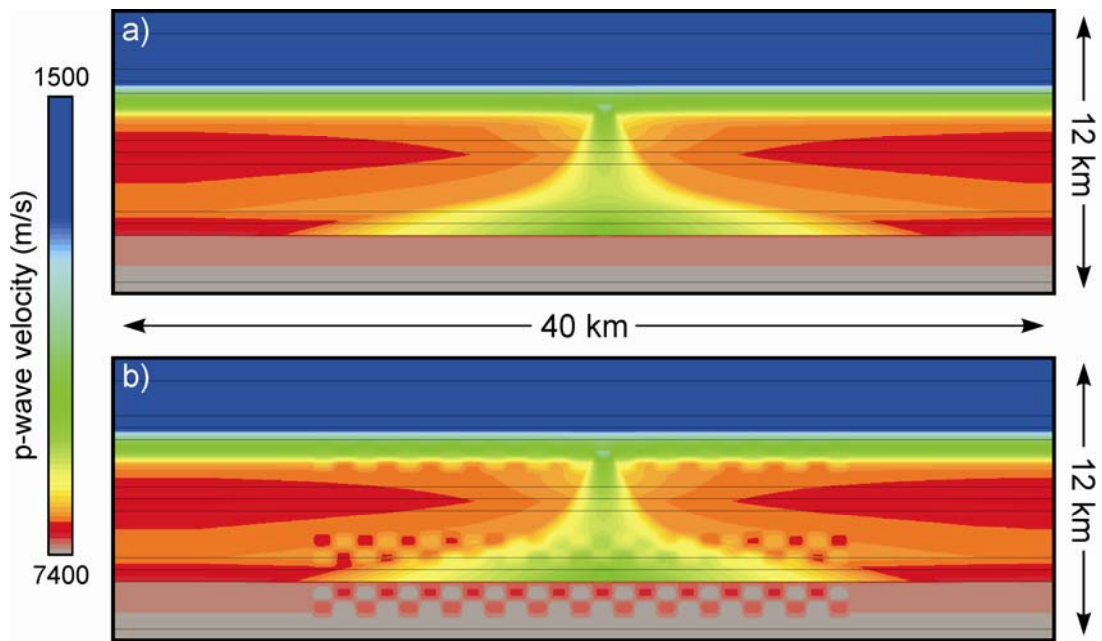


**Figure 11**

Vertical slice through 3D velocity model of the East Pacific Rise.

a) Long-wavelength background model.

b) With added checkerboards in upper crust, lower crust and uppermost mantle.

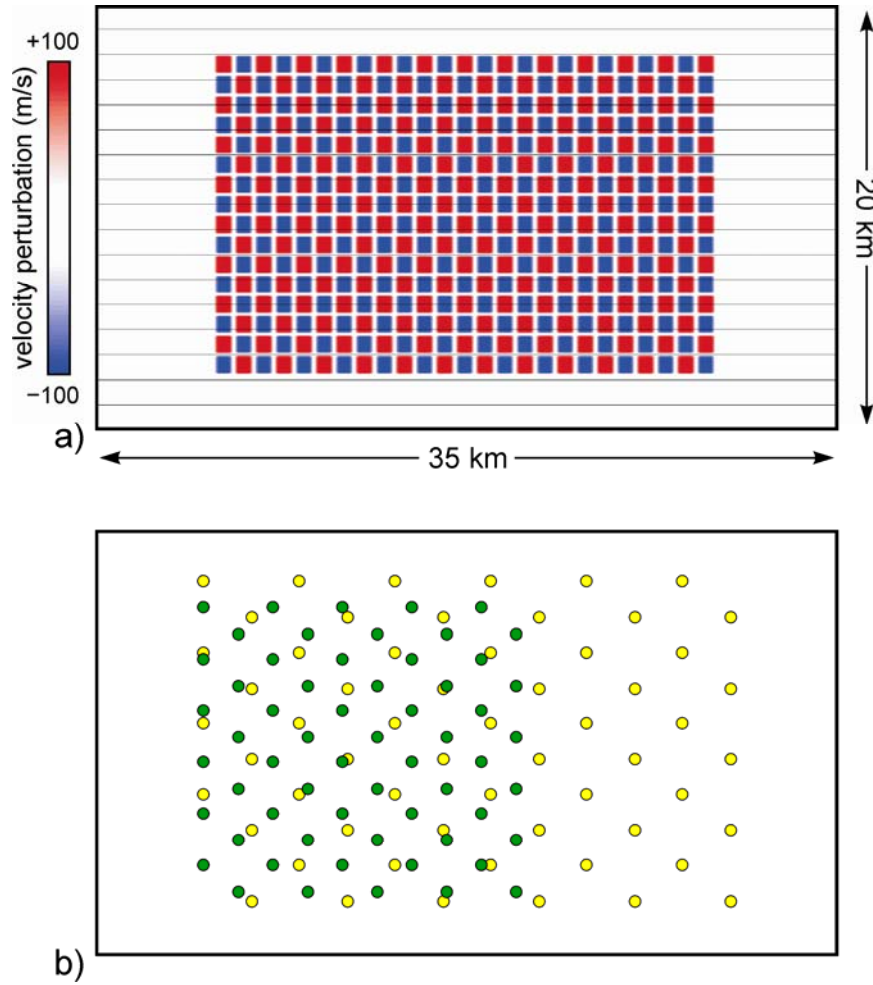


**Figure 12**

- a) Horizontal slice through the checkerboard perturbation in the uppermost mantle immediately below the Moho beneath the East Pacific Rise.
- b) Receiver locations on the seabed above the East Pacific Rise. The majority of the synthetic experiments used the array shown in yellow. The results shown in Fig. 14d used the reduced-area array shown in green.



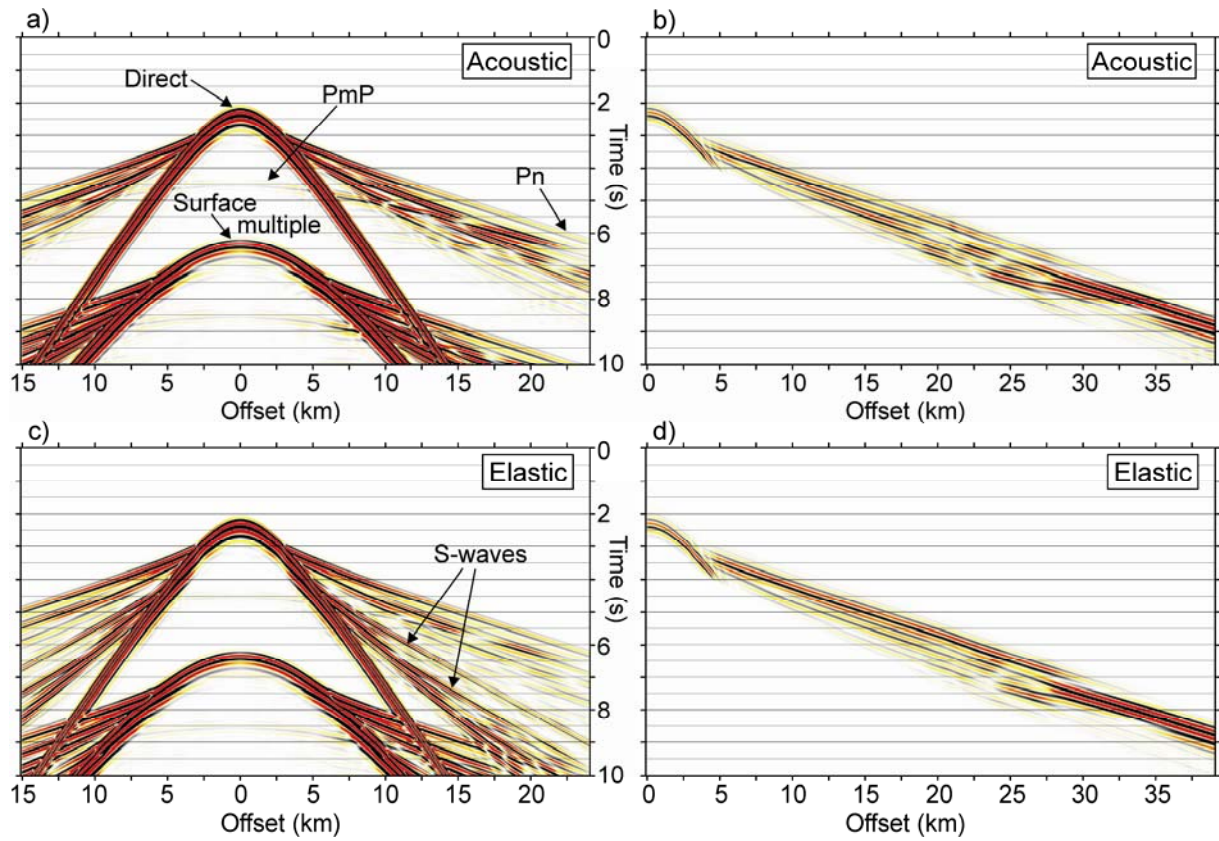


**Figure 13**

Synthetic seismograms generated using the model shown in Fig. 11.

a) Acoustic modelling. Trace amplitudes are weighted linearly with increasing offset but are otherwise shown at true amplitude.

b) Acoustic modelling after low-pass filtering and time windowing to match the bandwidth and data used for FWI. This record shows the full offset range of the data. The data have been amplitude normalised, trace by trace, after filtering and windowing – these are the data to which transmission FWI is typically applied.

c) Elastic modelling corresponding to (a).

d) Elastic modelling corresponding to (b).



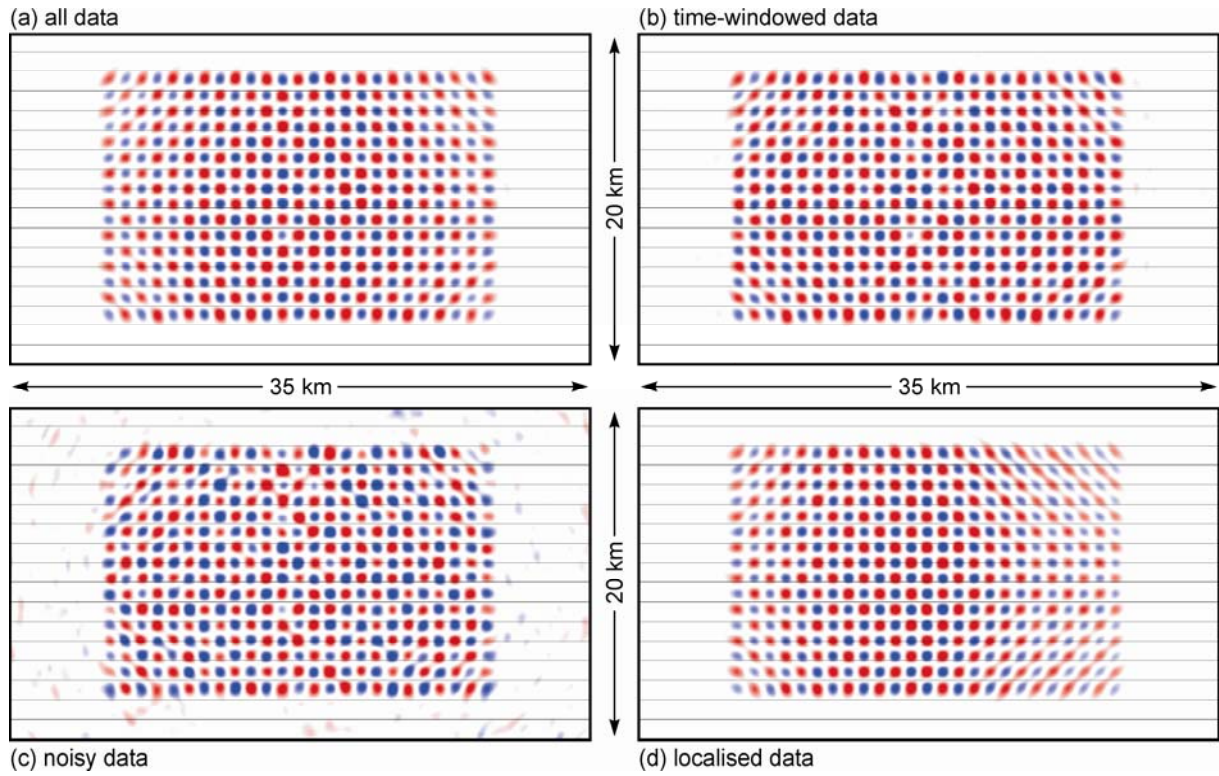


**Figure 14**

Recovered checkerboards in the mantle corresponding to Fig. 12.

a) Inverting all the data.

b) Inverting time-windowed data.

c) Inverting time-windowed data with added noise.

d) Inverting data from receivers that are clustered towards the left side of the model, green receivers in Fig. 12b.

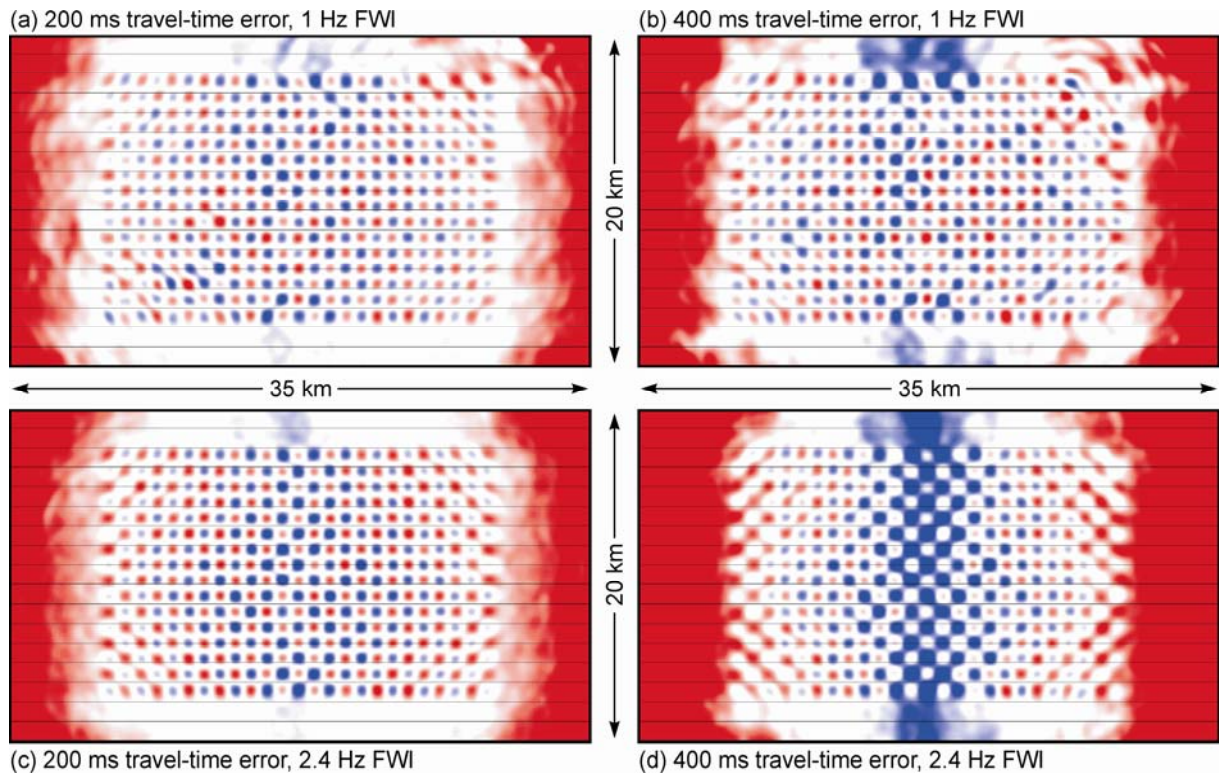


**Figure 15**

Recovered checkerboards obtained using starting models that have systematic errors.

- a) The starting model was everywhere fast, and the predicted travel times at 10 s were 200 ms early. The inversion started at 1 Hz.
- b) The starting model was everywhere fast, and the predicted travel times at 10 s were 400 ms early. The inversion started at 1 Hz
- c) Starting model as (a). The inversion started at 2.4 Hz.
- d) Starting model as (b). The inversion started at 2.4 Hz.

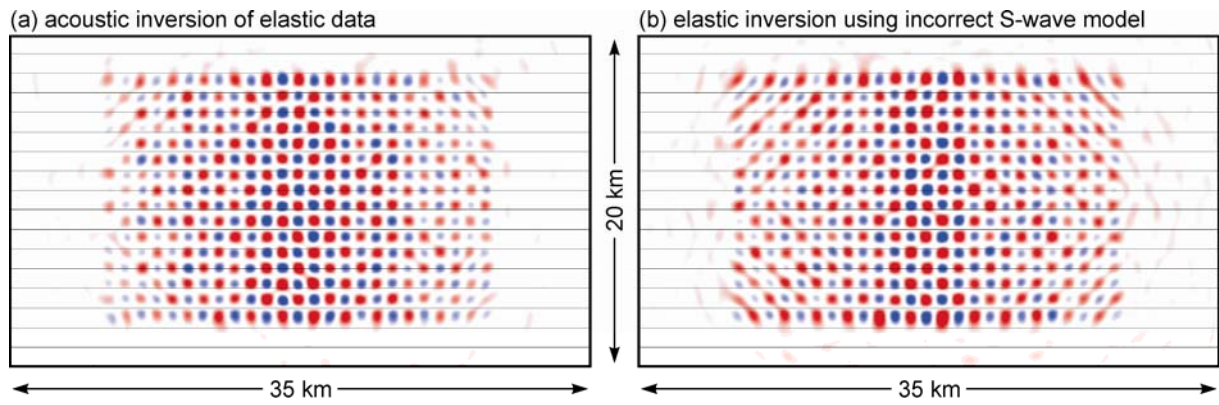


**Figure 16**

Recovered checkerboard obtained from elastic synthetic data.

a) Using acoustic inversion.

b) Using elastic inversion assuming a fixed relationship between P-wave and S-wave velocity.